

1

[ATLAS Semivisible Jets]

2

[Elena Laura Busch]

3

Submitted in partial fulfillment of the
requirements for the degree of
Doctor of Philosophy
under the Executive Committee
of the Graduate School of Arts and Sciences

4

5

6

7

8

COLUMBIA UNIVERSITY

9

2024

10

© 2024

11

[Elena Laura Busch]

12

All Rights Reserved

13

Abstract

14

[ATLAS Semivisible Jets]

15

[Elena Laura Busch]

16

Abstract of dissertation (place-holder).

Table of Contents

18	Acknowledgments	vii
19	Dedication	viii
20	Introduction or Preface	1
21	Chapter 1: The Standard Model	2
22	1.1 Phenomenology: Particles and Forces	2
23	1.1.1 Particles	2
24	1.1.2 Forces	3
25	1.2 QCD and Jets	6
26	1.3 Symmetries	7
27	1.3.1 Spontaneous Symmetry Breaking and The Higgs Mechanism	8
28	1.4 Experimental Validation of the Standard Model	9
29	1.5 Limitations of the Standard Model	10
30	Chapter 2: Physics Beyond the Standard Model	12
31	2.1 Hidden Valley Models	12
32	2.2 Dark QCD	13
33	2.3 Semi-visible Jets	14

34	Chapter 3: The Large Hadron Collider	16
35	3.1 Accelerator Physics	17
36	3.1.1 The Journey of a Proton	17
37	3.1.2 Magnets	18
38	3.2 Luminosity	19
39	3.3 LHC Timeline	22
40	Chapter 4: The ATLAS Detector	24
41	4.1 Coordinate System and Geometry	24
42	4.2 Inner Detector	26
43	4.2.1 Pixel Detector	26
44	4.2.2 Semiconductor Tracker	27
45	4.2.3 Transition Radiation Tracker	27
46	4.3 Calorimeters	28
47	4.3.1 Liquid Argon Calorimeter	29
48	4.3.2 Tile Calorimeter	32
49	4.4 Muon Spectrometer	33
50	4.5 Magnet System	35
51	4.6 Forward Detectors	36
52	4.7 Trigger and Data Acquisition	37
53	Chapter 5: Particle Reconstruction and Identification	39
54	5.1 Inner Detector Tracks	39
55	5.2 Photons and Electrons	40

56	5.3 Muons	42
57	5.4 Jets	44
58	5.4.1 Calorimeter Clusters	45
59	5.4.2 Particle Flow Reconstruction	45
60	5.4.3 Jet Clustering	45
61	5.4.4 Jet Substructure	45
62	5.5 Missing Transverse Energy	45
63	Conclusion or Epilogue	46
64	References	50
65	Appendix A: Experimental Equipment	54
66	Appendix B: Data Processing	55

List of Figures

68	1.1	Diagram of the 17 particles comprising the Standard Model	3
69	1.2	Fundamental particle interactions of the three fundamental forces described by the	
70		Standard Model [2].	5
71	1.3	An example Feynmann diagram of jet production	6
72	1.4	An illustration of the “hat shaped” potential of the Higgs field, resulting in a non-	
73		zero vacuum expectation value.	8
74	2.1	Illustration of the hidden valley potential	13
75	2.2	The massive mediator particle Z' of the s-channel realization of a HV model . . .	13
76	3.1	The LHC accelerator complex at CERN [27]	18
77	3.2	The octants of the LHC and location of various beam activities [26]. Stars indicate	
78		the locations of beam collisions, and the associated detectors recording the	
79		outcome of those collisions.	19
80	3.3	(Left) Total integrated luminosity over the course of Run 2. (Right) Average num-	
81		ber of $p\bar{p}$ interactions per bunch crossing in Run 2. Each curve is weighted by the	
82		integrated luminosity for the year.	21
83	3.4	Timeline of LHC and HL-LHC activities [29]. Integrated luminosity estimates are	
84		approximate, and not reflective of the exact amount delivered to each experiment. .	23
85	4.1	ATLAS coordinate system and geometry	26
86	4.2	A 3D visualization of the structure of the ID in the barrel region [33]	27
87	4.3	ATLAS calorimetery system [34]	28

88	4.4	Diagram of a segment of the EMB, demonstrating the accordion plate arrangement [35]	30
90	4.5	A LAr pulse as produced in the detector (triangle) and after shaping (curve) [35]	31
91	4.6	Readout gap structure in HEC [35]	31
92	4.7	TileCal wedge module [38]	33
93	4.8	Cross section view of the muon spectrometer system [39]	34
94	4.9	Layout of the barrel and endcap toroid magnets [32]	36
95	5.1	Graphic illustrating the various objects and high level features identified by ATLAS object reconstruction, and their interaction with different systems of the ATLAS detector [42]	40
98	5.2	Track reconstruction seeding, finding and fitting illustration [43]	41
99	5.3	Four types of muon track candidates [45].	42
100	5.4	Four types of muon track candidates [47].	44
101	5.5	The fragmentation and hadronization processes undergone by a quark produced in a proton-proton collision [49].	45
102			

List of Tables

104

Acknowledgements

105 Insert your acknowledgements text here. This page is optional, you may delete it if not

106 needed.

107

Dedication

108

Dedicated to my friends and family

109

Introduction or Preface

110 Insert your preface text here if applicable. This page is optional, you may delete it if not
111 needed. If you delete this page make sure to move page counter comment in thesis.tex to correct
112 location.

Chapter 1: The Standard Model

115 The Standard Model of particle physics is a universally accepted framework which explains
 116 the interactions of fundamental particles. All known fundamental particles, outlined in Figure
 117 1.1, are represented in the Standard Model. The model describes three of the four known forces:
 118 the electromagnetic force, the weak force, and the strong force. Gravity, the fourth fundamental
 119 force, is not addressed by the Standard Model. The Standard Model was primarily developed over
 120 the course of the 1960s and 1970s, by combining the work of many physicists into one coherent
 121 model. The Standard Model has been established as a well-tested theory by decades of experimen-
 122 tal physics research.

123 This chapter will seek to introduce the phenomenology and mathematical foundations of the
 124 Standard Model, and present the supporting experimental evidence. Phenomenon which are unex-
 125 plained by the Standard Model such as gravity will be considered at the end of the chapter, leading
 126 to an exploration of theories beyond the Standard Model in the subsequent chapter.

127 **1.1 Phenomenology: Particles and Forces**

128 1.1.1 Particles

129 A classic representation of the particles comprising the Standard Model is shown in Figure
 130 1.1. The two primary particles classes are bosons (gauge bosons and the scalar Higgs boson) and
 131 fermions (leptons and quarks). The bosons are carriers of fundamental forces, while the fermions
 132 are the building blocks of matter. Fermions are sorted into three *generations*, and each fermion is
 133 identified by a unique *flavor*.

134 Each entry in the table in Figure 1.1 is accompanied by 3 characteristic numbers: mass, charge,
 135 and spin. The mass of each particle is determined to limited precision by experimental observa-

Standard Model of Elementary Particles

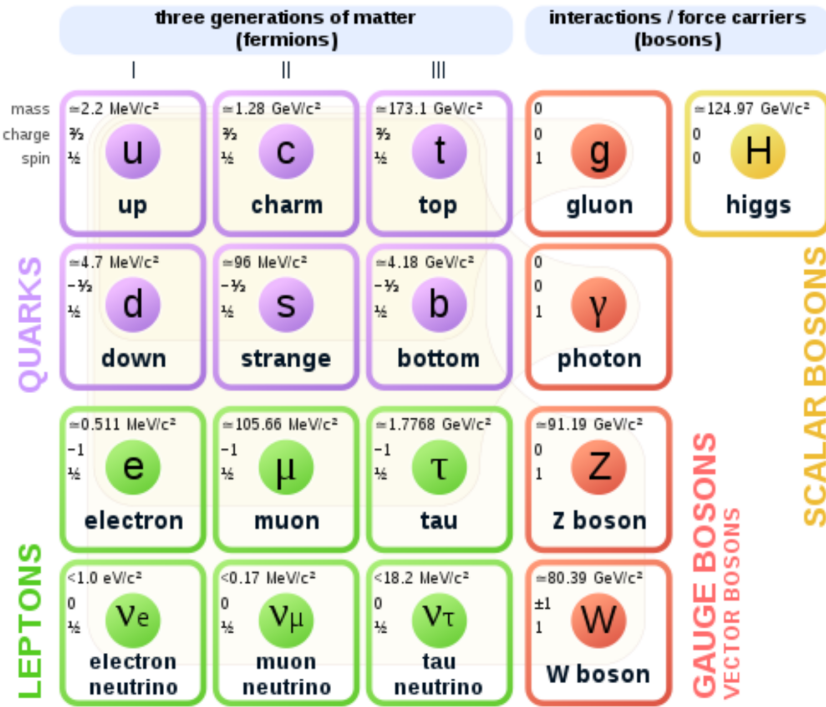


Figure 1.1: Diagram of the 17 particles comprising the Standard Model

136 tion, with the exception of photons and gluons which are known to be massless. Charge refers to
 137 the electromagnetic charge in the case of leptons and W bosons, and to color charge in the case
 138 of quarks and gluons. Spin is an intrinsic form of angular momentum carried by fundamental
 139 particles; all fermions have half integer spin, while bosons have integer spin.

140 Each particle is also known to have an *antiparticle*. Each antiparticle has the same mass but the
 141 opposite charge of their Standard Model counter part; for example, the antiparticle of the electron
 142 is the positron, which has all the same properties but a positive charge. The photon, Z boson,
 143 and Higgs are each their own antiparticle. The nature of antineutrinos is an open question driving
 144 neutrino physics research, as it is not currently known whether neutrinos are their own antiparticle.

145 1.1.2 Forces

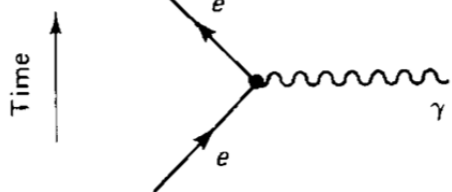
146 The three fundamental forces explained by the Standard Model are the electromagnetic force,
 147 the strong force, and the weak force. The photon is the carrier of the electromagnetic force, which

¹⁴⁸ dictates the nature of interactions between electrically charged particles, and is widely covered by
¹⁴⁹ introductory physics courses. The electromagnetic force has an infinite interaction range, a result
¹⁵⁰ of the massless and non-self interaction nature of the photon. The electromagnetic interaction is
¹⁵¹ described by the theory of quantum electrodynamics (QED).

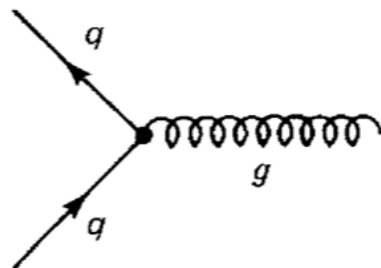
¹⁵² The weak force gives rise to atomic radiation and decay. It allows for the processes of beta
¹⁵³ decay, which enables conversion between neutrons and protons within the nucleus of an atom. In
¹⁵⁴ the process of beta decay, a proton decays into a neutron, a positron, and a neutrino; or, a neutron
¹⁵⁵ decays into a proton, an electron and an antineutrino. The weak interaction allows for quark flavor
¹⁵⁶ mixing, the which enables beta decay. The W^+ , W^- , and Z^0 are the force carriers of the weak force.
¹⁵⁷ The effective range of the weak force is limited to subatomic distances, as a result of the massive
¹⁵⁸ nature of the mediator bosons. The unified theory of the electroweak interaction posits that at high
¹⁵⁹ enough energies the electromagnetic interaction and the weak force merge into the same force.
¹⁶⁰ This threshold is termed the unification energy and calculated to be about 246 GeV [1].

¹⁶¹ The strong force confines quarks into hadron particles, such as protons and neutrons. The
¹⁶² strong force also allows for the creation of atomic nuclei by binding protons and neutrons together,
¹⁶³ and is generally referred to as the “nuclear force” in this context. The gluon is the mediator of
¹⁶⁴ the strong force, which is a short-range force which acts at subatomic distances on the order of
¹⁶⁵ 10^{-15} m. At this range, the strong force is about 100x as strong as the electromagnetic force,
¹⁶⁶ which allows for the creation of positively charged nuclei [2]. The strong force is described by the
¹⁶⁷ theory of quantum chromodynamics (QCD). In the same way that QED dictates the interaction of
¹⁶⁸ electrically charges particles, QCD dictates the interactions of *color-charged* particles. Due to the
¹⁶⁹ particular importance of QCD in this thesis, this topic will be explored in detail in section 1.2.

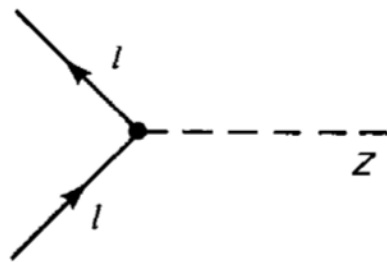
¹⁷⁰ The fundamental Feynmann diagram for each of the three forces discussed here is depicted
¹⁷¹ in Figure 1.2. The fourth fundamental force, gravity, is not currently explained by any known
¹⁷² mechanism within the Standard Model.



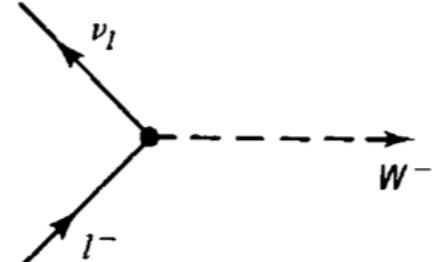
(a) The electromagnetic force



(b) The strong force



(c) The neutral weak force



(d) The charged weak force

Figure 1.2: Fundamental particle interactions of the three fundamental forces described by the Standard Model [2].

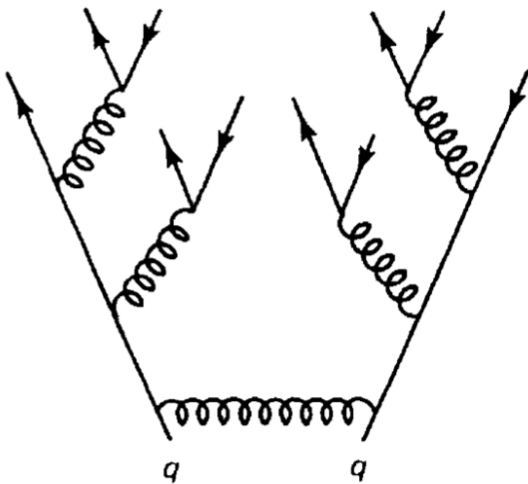


Figure 1.3: An example Feynmann diagram of jet production

¹⁷³ 1.2 QCD and Jets

¹⁷⁴ While there is only one type of electric charge, there are three types of color charge; red, green,
¹⁷⁵ and blue. In the process $q \rightarrow q + g$, the color of the quark can change. In order to conserve color
¹⁷⁶ charge, gluons are bicolored, and always carry some positive color charge and some negative color
¹⁷⁷ charge.

¹⁷⁸ Color charged particles can only exist in bound states which result in a neutral total color
¹⁷⁹ charge, a principle known as confinement. This requires that quarks and gluons exist in group
¹⁸⁰ states known as hadrons; either mesons in the case of two quarks or baryons in the case of three
¹⁸¹ quarks. When a quark is separated from a hadron, confinement dictates that other colored objects
¹⁸² are produced around the quark to obey confinement. An example of this process is shown in
¹⁸³ Figure 1.3. This ensemble of objects, generally a mixture of quarks and gluons, is termed a *jet*.
¹⁸⁴ Jets are among the most common phenomenon observed by detectors at hadron colliders, and their
¹⁸⁵ complex structure makes them a key focus of many physics analyses.

186 **1.3 Symmetries**

187 The Standard Model is a renormalizable quantum field theory that obeys the local symmetry

188 G_{SM} :

$$G_{SM} = SU(3)_C \times SU(2)_L \times U(1)_Y. \quad (1.1)$$

189 The $SU(3)_C$ symmetry component represents the non-Abelian gauge group of QCD. There
190 are 8 generators for the $SU_C(3)$ group which correspond to 8 types of gluon, each representing a
191 different superposition of color charge [3]. The $SU(2)_L \times U(1)_Y$ symmetry group represents the
192 electroweak sector of the Standard Model, which can be spontaneously broken into the electromag-
193 netic and weak sectors. There are 4 generators for this group, which correspond to four massless
194 gauge bosons W^1 , W^2 , W^3 , and B . From these massless gauge bosons are formed the massive
195 mediators of the weak force, the W^- , W^+ and Z^0 bosons, and the massless electromagnetic force
196 carrier, the photon γ . Spontaneous symmetry breaking and the process by which gauge bosons
197 acquire mass will be addressed in section 1.3.1.

198 Noether's theorem [4] stipulates that any continuous symmetry is associated with a conserved
199 quantity. In the Standard Model, this means that the $SU(3)_C$ symmetry gives rise to conservation of
200 color charge. The $SU(2)_L \times U(1)_Y$ symmetry gives rise to conservation of electromagnetic charge.
201 Conservation of spin results from the Poincaré symmetry described by the theory of special rela-
202 tivity, which combined with Noether's theorem gives us the conversation of energy, momentum,
203 and angular momentum.

204 The SM Lagrangian is invariant under CPT symmetry, or charge, parity, and time reversal.
205 Charge conjugation (C) transform a particle into it's corresponding antiparticle by reversing the
206 charge and other quantum numbers. Parity conjugation (P) reverses spatial coordinates, which
207 transforms left-handed particles into right-handed particles and vice-versa. Time reversal (T) is
208 the theoretical process of reversing time. The L subscript in the $SU(2)_L$ group indicates that this
209 symmetry only applies to left-handed fermions. As a result, the $W^{1,2,3}$ gauge bosons of $SU(2)_L$

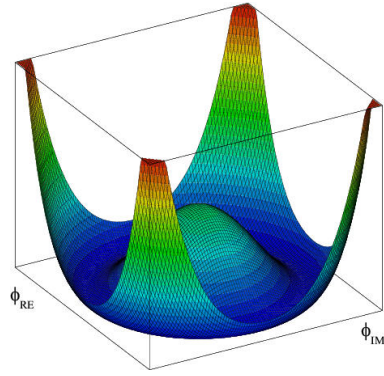


Figure 1.4: An illustration of the “hat shaped” potential of the Higgs field, resulting in a non-zero vacuum expectation value.

only interact with left handed particles, a process which maximally violates P-symmetry in the weak force. A small amount of the CP symmetry violation is also observed in the Standard Model, through the decays of strange flavored mesons [5]. The CPT theorem posits that the violation of CP symmetry implies that T-symmetry must also be violated, so that CPT is a preserved symmetry.

1.3.1 Spontaneous Symmetry Breaking and The Higgs Mechanism

Spontaneous symmetry breaking is the process by which a Lagrangian obeys a symmetry at high energies, but exhibits asymmetric behavior at lower energies. The electroweak symmetry group is spontaneously broken as $SU(2)_L \times U(1)_Y \rightarrow U(1)_{EM}$. The quantity conserved by the $SU(2)_L$ symmetry is weak isospin $T_{1,2,3}$, while the quantity conserved by $U(1)_Y$ symmetry is weak hypercharge Y . Below very high energies, the presence of the Higgs field causes the electroweak symmetry to break. The Higgs field is scalar field which forms a complex doublet of the $SU(2)$ symmetry group, with four degrees of freedom. The shape of the Higgs field potential, shown in Figure 1.4, results in a ground state with a non-zero vacuum expectation value; thus the Higgs field takes a non-zero value throughout all space, which breaks the symmetry of the weak isospin $SU(2)$ group.

The interaction with the Higgs field mixes the four massless gauge bosons $W^{1,2,3}$ and B . Three Higgs field degrees of freedom mix with the massless gauge bosons, resulting in three massive gauge bosons W^- , W^+ and Z^0 . The massless photon γ is created from the components of the

228 massless gauge bosons which do not interact with the Higgs field. The scalar Higgs boson arises
229 from the one unmixed degree of freedom the Higgs field. Spontaneous symmetry breaking also
230 violates the conservation of weak isospin and weak hypercharge, leaving only electromagnetic
231 charge ($Q = T_3 + \frac{1}{2}Y$) as a conserved quantity associated with the $U(1)_{EM}$ symmetry.

232 **1.4 Experimental Validation of the Standard Model**

233 The theoretical framework of the Standard Model coalesced into a unified theory in the mid-
234 20th century. A cascade of discoveries providing empirical evidence for the model followed
235 closely. In the 1960s, three quarks (up, down and strange) and four leptons (electron, muon,
236 and their associated neutrinos) were the known particulate building blocks of matter and the Stan-
237 dard Model. The discovery of the charm quark in 1974, through the observation of the J/ψ meson
238 [6][7], confirmed the existence of a fourth quark flavor. The discovery of the τ in 1975 [8] provided
239 the first evidence of a 3rd generation of matter. This was quickly followed by the observation of
240 the Υ meson in 1977 [9], which provided evidence for the existence of a fifth quark, the b quark
241 (bottom, or beauty). The existence of a 3rd generation of fermion also explained the observation
242 of CP violation in the weak force, as it allowed for the addition of a complex phase in the CKM
243 matrix (a unitary matrix which describes flavor mixing in the weak interaction). The top quark
244 (t) and tau neutrino (ν_τ) were predicted at this point as the final building blocks of three complete
245 generations of fermions, and they were discovered by experimental observation around the turn of
246 the 21st century [10] [11] [12].

247 The W and Z bosons were predicted by the Standard Model, but to observe them required the
248 construction of a particle accelerator powerful enough to produce them. They were finally observed
249 at CERN in 1983 by the UA1 and UA2 experiments [13] [14] at the newly constructed Super Proton
250 Synchrotron (SPS). Their masses were observed to be compatible with the masses predicted by the
251 Standard Model nearly a decade earlier. The final missing piece then was confirming the existence
252 of the Higgs, which again required the construction of a newer and more powerful collider. CERN
253 achieved this with the construction of the Large Hadron Collider (LHC), and in 2012 the ATLAS

254 and CMS experiments announced the discovery of the Higgs particle [15] [16].

255 **1.5 Limitations of the Standard Model**

256 While the Standard Model has enjoyed decades of experimental results which confirm its pre-
257 dictions, there are several glaring shortcomings. The observed phenomenon for which the Standard
258 Model provides no explanation are summarized below.

- 259 • Gravity - the Standard Model does not account for the fourth fundamental force of gravity.
- 260 • Dark Matter - there is no viable candidate to explain the existence of dark matter, a non-
261 interacting form of matter which must exist to account for gravitational observations which
262 cannot be explained by general relativity, such as the motion of galaxies, gravitational lens-
263 ing, and the structure of the universe [17].
- 264 • Matter-Antimatter asymmetry - the level of CP violation in the Standard Model isn't suf-
265 ficient to explain the large discrepancy between the amount of matter and the amount of
266 antimatter in the universe today, and the origins of this imbalance are not understood.
- 267 • Neutrino masses - the Standard Model assumes that neutrinos are massless and provides
268 no mechanism for them to acquire mass. However, observations of neutrino oscillations
269 indicates they posses some small non-zero mass [18].

270 In addition to these unexplained natural phenomenon, there are several questions about the
271 *naturalness* of the Standard Model. The principle of naturalness states that dimensionless ratios
272 between physical constants should be of order 1, and that nature should not be arbitrarily fine-
273 tuned. While this is largely an aesthetic argument, it points to many aspects of the Standard Model
274 for which there exists no natural explanation.

- 275 • Strong CP - while CP symmetry is violated in the weak force, observations indicate that it
276 is preserved by the strong force [19]. The Standard Model predicts that CP violation in the

277 strong force is possible. There is no principle which motivates this incongruity between the
278 weak force and strong force.

- 279 • Hierarchy Problem - The wide range of masses for elementary particles and the wide range of
280 scales at which the four fundamental forces operate is not motivated by the SM. Specifically,
281 it is not understood why the Higgs mass is observed to be well below the Plank scale λ ,
282 which is the energy level at which the effects of quantum gravity become significant. QFT
283 indicates that the Higgs mass is determined by contributions from all energy scales including
284 λ , meaning that its observed mass is inexplicably small.

285 The limitations of the Standard Model provide a road map for theoretical and experimental
286 particle physicists, who seek to develop new theories which account for these observations, and
287 then to find evidence which might support these *Beyond the Standard Model* (BSM) theories. The
288 next chapter will introduce the BSM theories which motivate the physics search presented in this
289 thesis.

Chapter 2: Physics Beyond the Standard Model

292 In light of the various phenomenon unexplained by the Standard Model, physicists have pro-
 293 posed various extensions to the Standard Model, collectively termed *Beyond the Standard Model*
 294 (BSM) theories. A particular focus of the physic programs at the Large Hadron Collider (LHC) are
 295 BSM models which suggest dark matter candidate particles. If these particles couple to Standard
 296 Model, they could be produced and observed at the LHC.

297 **2.1 Hidden Valley Models**

298 Hidden Valley (HV) models are a category of BSM models that allow for dark matter (DM)
 299 production at the LHC. They extend the Standard Model with an additional non-Abelian gauge
 300 group [20]. This introduces the possibility of a complex dark sector, which mirrors the complexities
 301 of Standard Model QCD, and introduces the possibility of dark quarks and gluons. The term
 302 “hidden valley” refers to the idea that the DM is hidden from the SM by a high-energy barrier, as
 303 illustrated in Figure ???. The dark sector is assumed to communicate with the Standard Model via
 304 a “portal”, or “messenger particle”, that can interact with both Standard Model and HV forces. For
 305 the s-channel scenario, the portal is considered to be a new massive mediator particle Z' .

306 The portal particle allows for the production of dark sector particles at hadron colliders. If
 307 dark quarks are produced via the decay $Z' \rightarrow q_D q_D$ they can hadronize and form dark jets. The
 308 properties of the dark jets are determined by the dynamics of the dark sector, which are explored in
 309 the subsequent section. Depending on the details of the model, the jets formed by the dark hadrons
 310 can be categorized as fully dark, semi-visible, leptonic, emerging, or other [20].

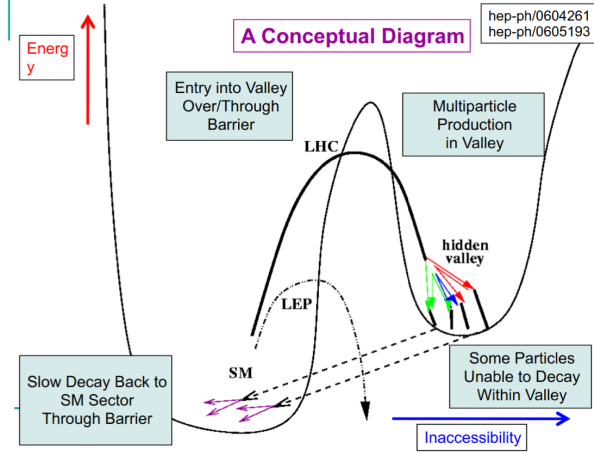


Figure 2.1: Illustration of the hidden valley potential

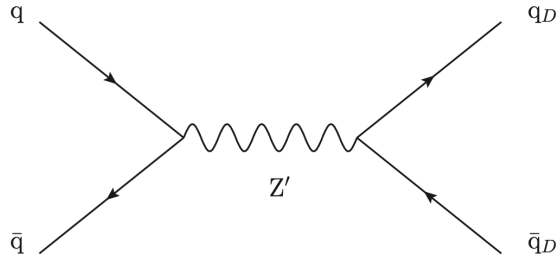


Figure 2.2: The massive mediator particle Z' of the s-channel realization of a HV model

311 2.2 Dark QCD

312 The theoretical underpinning of the semi-visible jet phenomenology is a dark sector with a
 313 gauge group $SU(N_d)$ leading to confinement at a scale Λ_d . For illustration, let's consider the
 314 case of an $SU(2)_d$ gauge theory, which gives rise to two dark fermionic generations $\chi_a = \chi_1, \chi_2$.
 315 Following the work of Timothy Cohen, et.al. we can write the fundamental dark Lagrangian as:

$$\mathcal{L}_{dark} \supset -\frac{1}{2} \text{Tr } G_{\mu\nu}^d G^{d\mu\nu} - \bar{\chi}_a (i \not{D} - M_{d,a}) \chi_a \quad (2.1)$$

316 The first term allows for the dark gluons to self-interact, while the second term enables the dark
 317 quarks to hadronize and acquire mass. The dark quarks are assumed to have a common mass M_d .
 318 The coupling strength of the strongly interacting dark quarks is termed α_d . At the confinement

319 scale Λ_d , the dark quarks can form bound states. At the scale $M_d \approx \Lambda_d$ a QCD-like show occurs.

320 The properties of the hadrons formed by the dark quarks are of particular importance to the
321 observed dark QCD dynamics. Dark-isospin number $U(1)_{1-2}$ and dark-baryon number $U(1)_{1+2}$
322 are accidental symmetries of the theory which determine the stability of the hadrons. In the case
323 of two dark flavors, six dark hadrons can be formed: four mesons ($\chi_1\bar{\chi}_1$, $\chi_2\bar{\chi}_2$, $\chi_1\bar{\chi}_2$, $\bar{\chi}_1\chi_2$) and
324 two baryons ($\bar{\chi}_1\bar{\chi}_2$, $\bar{\chi}_1\bar{\chi}_2$). The mesons $\chi_1\bar{\chi}_2$ and $\bar{\chi}_1\chi_2$ are charged under dark-isospin and will be
325 stable if this symmetry is unbroken. The baryons would also be stable as they are charged under
326 the dark-baryon number. These four stable hadrons become dark matter candidates of the theory.
327 The $\chi_1\bar{\chi}_1$ and $\chi_2\bar{\chi}_2$ mesons are not charged under either symmetry and are thus expected to decay.
328 The unstable mesons can decay into stable dark mesons, or into an off-shell Z' . The off-shell Z'
329 will then decay into two DM quarks or two SM quarks, and its products will continue to shower
330 until the final state particles are stable.

331 The number of stable and unstable dark states varies substantially depending on the details
332 of the model. The model discussed above can be generalized from $SU(2)_d$ to $SU(N)_d$, with any
333 number of colors N_c or flavors N_f . This affects the ratio of possible stable to unstable mesons,
334 which can directly impact the amount of missing energy. The fraction of missing energy is a
335 variable in many dark QCD models, and is especially important in the case of semi-visible jets.

336 2.3 Semi-visible Jets

337 A “semi-visible jet” occurs when the heavy Z' messenger particle decays into dark quarks,
338 which then hadronize in a QCD-like shower. If some of the dark hadrons are stable while others
339 decay to SM quarks via the off-shell Z' , a collimated mixture of visible and dark matter is formed
340 – this is termed a semi-visible jet. If the Z' messenger particle is produced at rest, the two jets will
341 be back-to-back in the transverse plane. If there is an imbalance in the amount of invisible particles
342 between the two jets, one of the jets will be observed to be aligned with missing transverse energy.

343 While there are a myriad of HV and dark QCD models, a handful of model parameters are most
344 important in determining the observable of these showers within a particle detector. The coupling

345 strength α_d is one of the most important, as it controls the fraction of dark hadrons emitted in the
346 shower and their average p_T . The mass of the dark quarks directly impacts the jet mass. If the
347 masses of the dark quark flavors are comparable, the ratio of stable to unstable dark hadrons will
348 be approximately 1:1. However, if there is a mass splitting, stable or unstable dark hadrons may
349 be favored, which impacts the amount of missing energy observed.

350 The ratio of stable to unstable dark hadrons in the shower is a critical variable for capturing the
351 behavior of dark showers. This value is termed r_{inv} :

$$r_{inv} = \frac{\# \text{ of stable hadrons}}{\# \text{ of hadrons}} \quad (2.2)$$

352 Events containing jets aligned with missing transverse momentum are generally considered to
353 be misreconstructed by other DM searches, and therefore discarded. This class of final states is
354 therefore largely uncovered by existing DM searches. The nature of the dark hadron shower is
355 determined by the following parameters: the Z' mass $m_{Z'}$, the Z' couplings to visible and dark
356 quarks g_q and g_{q_D} , the number of dark colors and flavors, the characteristic scale of the dark sector
357 confinement Λ_D , the scale of the dark hadrons m_D , and the average fraction of stable hadrons in
358 the decay r_{inv} . The coupling to SM quarks determines the Z' production cross section.

Chapter 3: The Large Hadron Collider

361 The Large Hadron Collider (LHC) is a 26.7 km circular high-energy particle accelerator, span-
 362 ning the Swiss-French border near the city of Geneva, Switzerland [21]. The LHC occupies the
 363 tunnel constructed in 1989 for the Large Electron-Positron (LEP) Collider, and reaches a maxi-
 364 mum depth of 170m below the surface. The LHC is operated by the European Organization for
 365 Nuclear Research (CERN), the largest international scientific collaboration in the world.

366 The LHC accelerates protons and heavy ions, and collides them at four interaction points
 367 around the ring, with a design center-of-mass energy per collision of $\sqrt{s} = 14$ TeV. Each interaction
 368 point is home to one of four detector experiments, which study the products of the collisions. The
 369 largest of these experiments is the ATLAS detector, a general purpose detector designed to study
 370 the Standard Model and search for new physics that could be produced in LHC collisions [22].
 371 The CMS detector is another general purpose detector, designed and operated independently of the
 372 ATLAS detector, but intended to probe the same range of physics [23]. The ALICE experiment is
 373 a dedicated heavy ion experiment, and the LHC-b experiment is a dedicated *b*-physics experiment
 374 [24] [25].

375 This chapter will cover the multi-component accelerator complex powering the LHC, the state-
 376 of-the-art magnets which steer the particle beams, measurements of the intensity and number of
 377 collisions produced by the LHC, and finally an overview of LHC activities in the past, present, and
 378 future.

379 **3.1 Accelerator Physics**

380 **3.1.1 The Journey of a Proton**

381 From 2010 - 2018, the protons which fed the LHC started as hydrogen gas. The electrons were
382 removed from the hydrogen atoms through the use of strong electric fields. The linear accelerator
383 LINAC2 then accelerated the protons to an energy of 50 MeV. Between 2018 and 2020, LINAC2
384 was replaced with LINAC4, which instead accelerates H^- ions, hydrogen atoms with two electrons.
385 LINAC4 is capable of accelerating the H^- ions to 160 MeV. Before injection to the next part of
386 the acceleration chain, both electrons are stripped from the H^- ions, leaving just protons. From
387 here the protons enter the Proton Synchrotron booster, where they are accelerated up to 1.4 GeV of
388 energy. Subsequently they are sorted into bunches separated in time by 25 ns, where each bunch
389 contains approximately 10^{11} protons. Next the bunches pass through the Proton Synchrotron (PS)
390 and the Super Proton Synchrotron (SPS), where they reach energies of 25 GeV and 450 GeV
391 respectively. Finally they are injected into the LHC as two beams traveling in opposite direction.
392 The original design allowed each beam to be accelerated up to 7 TeV of energy. Due to limitations
393 in the performance of the superconducting LHC magnets, the highest energy actually achieved by
394 the LHC beams during Run 2 was 6.5 TeV, giving a collision center-of-mass energy of $\sqrt{s} = 13$
395 TeV [26]. Figure 3.1 shows the full LHC accelerator complex.

396 Acceleration in the LHC is performed by eight radio frequency (RF) cavities located around the
397 ring. Each RF cavity produces a 2 MV electric field oscillating at 40 MHz. The 40MHz oscillation
398 produces a point of stable equilibrium every 2.5 ns. These points of equilibrium are synchronized
399 with the occurrence of the proton bunches produced in the PS – a proton bunch occupies one out
400 of every ten points of stable equilibrium, such that the bunches maintain a 25 ns spacing [26].

401

The CERN accelerator complex Complexe des accélérateurs du CERN

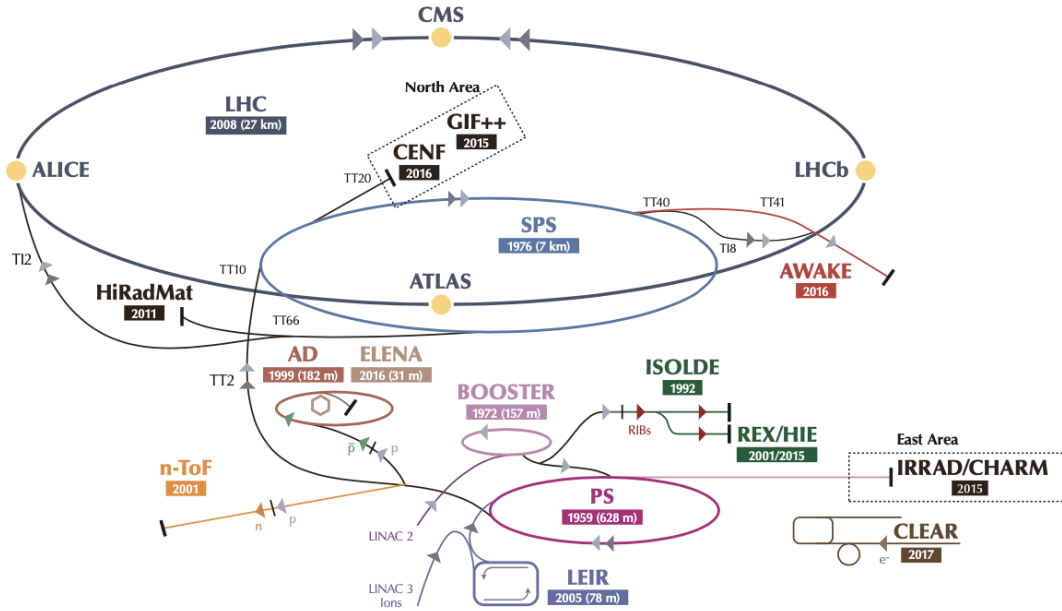


Figure 3.1: The LHC accelerator complex at CERN [27]

402 3.1.2 Magnets

403 In addition to the acceleration cavities, the LHC houses 9593 superconducting magnets which
 404 direct and focus the proton beam on its 27 kilometer journey. The magnets are comprised of super-
 405 conducting Niobium-Titanium coils cooled to 1.9K by superfluid helium. As the beams approach
 406 one of the four collision points around the ring, multipole magnets focus and squeeze the beam for
 407 optimal collisions [26].

408 The LHC is divided into sections, where each section contains an arc and a straight insertion. The arcs are composed of 1232 large dipole magnets which bend the beam
 409 to follow the roughly circular 27 km path. The main dipoles generate powerful 8.3 tesla magnetic
 410 fields to achieve this bend. Each dipole magnet is 15 meters long and weighs 35 tonnes. The
 411 dipoles work in conjunction with quadrupole magnets, which keep the particles in a focused beam,
 412 and smaller sextupole, octupole and decapole magnets which tune the magnetic field at the ends of
 413 the dipole magnets [28].

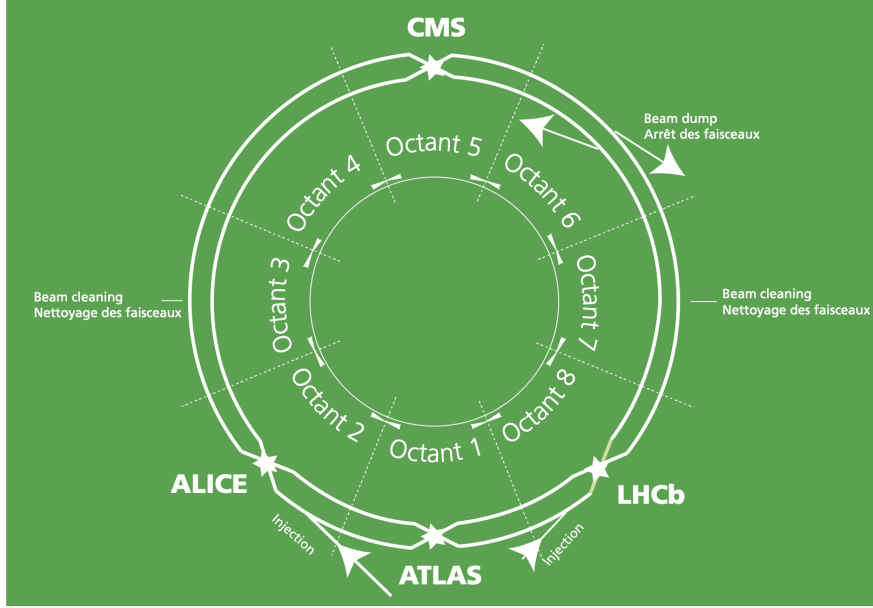


Figure 3.2: The octants of the LHC and location of various beam activities [26]. Stars indicate the locations of beam collisions, and the associated detectors recording the outcome of those collisions.

415 The straight insertion sections have different purposes depending on their location around the
 416 ring: beam collisions, beam injection, beam dumping, or beam cleaning. At the four collision
 417 points, insertion magnets squeeze the beam to ensure a highly focused collision. This is accom-
 418 plished with a triplet of quadrupole magnets, which tighten the beam from 0.2 millimeters to just
 419 16 micrometers in diameter. Insertion magnets also clean the beam, which prevents stray particles
 420 from hitting sensitive components throughout the LHC. When the LHC is ready to dispose of a
 421 beam of particles, beam dump magnets deflect the path of the beam into a straight line towards
 422 a block of concrete and graphite that stops the beam. A dilution magnet then reduces the beam
 423 intensity by a factor of 100,000 before the final stop [28]. Figure 3.2 shows the locations various
 424 beam activities.

425 3.2 Luminosity

426 Collisions at the LHC occur when the two beams of proton bunches cross at one of the four
 427 interaction points. The intensity of collisions is described by the instantaneous luminosity, the

428 formula for which is given in equation 3.1.

$$L = \frac{fN_1N_2}{4\pi\sigma_x\sigma_y} \quad (3.1)$$

429 Here f is the revolution frequency, N_1 and N_2 are the number of particle per bunch for each
430 beam, and σ_x , σ_y are the horizontal and vertical beam widths.

431 The instantaneous luminosity gives the number of the collisions that could be produced at the
432 interaction point per unit of cross-sectional area per unit of time, generally expressed in $\text{cm}^{-2}\text{s}^{-1}$.
433 The integrated luminosity is obtained by integrating the instantaneous luminosity over a given
434 block of time, and measures the total number of collisions which have occurred during that op-
435 eration period. The total integrated luminosity is directly correlated with the size of the datasets
436 collected by the LHC experiments. Total integrated luminosity for Run 2 is illustrated in Figure
437 3.3.

438 High levels of instantaneous luminosity result in multiple pp collisions per bunch crossing,
439 which leads to an effect known as *pileup*. Pileup poses a challenge for detector physics, as recon-
440 structing the products of multiple simultaneous events is far more challenging than reconstructing
441 a single event with no pileup. Pileup conditions vary from year-to-year and run-to-run of LHC op-
442 eration, and the impact of these conditions are taken into account when analyzing the data, as will
443 be discussed further in Chapter 5. Measurement of pileup conditions during Run 2 are illustrated
444 in Figure 3.3.

445 The design peak luminosity of the LHC is $1.0 \times 10^{34} \text{ cm}^{-2}\text{s}^{-1}$. During Run 1 of the LHC the
446 peak instantaneous luminosity was $0.8 \times 10^{34} \text{ cm}^{-2}\text{s}^{-1}$. Over the course of Run 1 the LHC collected
447 a total integrated luminosity of 5.46 fb^{-1} at $\sqrt{s} = 7 \text{ TeV}$, and 22.8 fb^{-1} at $\sqrt{s} = 8 \text{ TeV}$. Following the
448 first long shutdown and upgrade phase of operations, the LHC achieved a center of mass energy
449 $\sqrt{s} = 13 \text{ TeV}$ at the beginning of Run 2 in 2015. The LHC was also able to deliver 2.0×10^{34}
450 $\text{cm}^{-2}\text{s}^{-1}$ peak instantaneous luminosity, double the design value. During LHC Run 2, from 2015-
451 2018, the LHC delivered 156 fb^{-1} of integrated luminosity for proton-proton collisions. Run 3 of

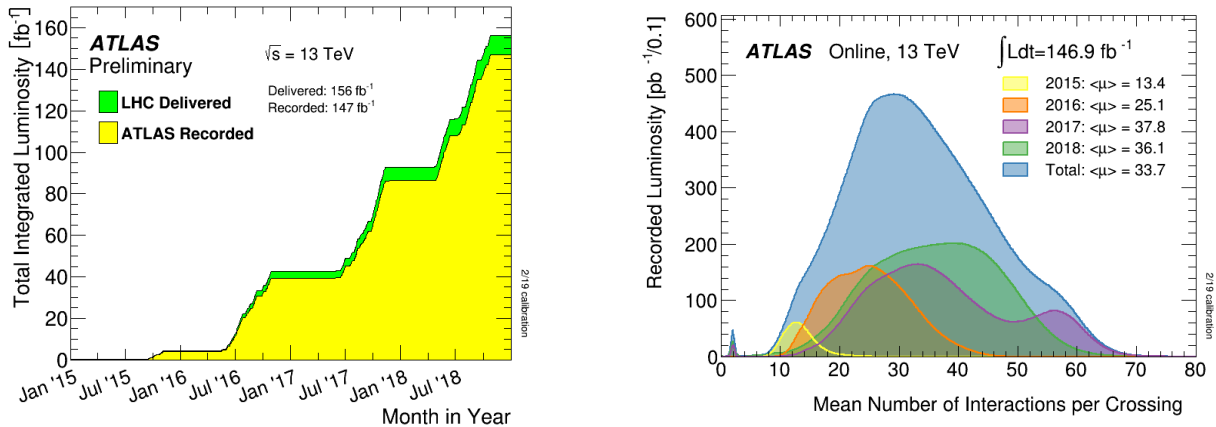


Figure 3.3: (Left) Total integrated luminosity over the course of Run 2. (Right) Average number of pp interactions per bunch crossing in Run 2. Each curve is weighted by the integrated luminosity for the year.

452 the LHC began in 2022, and is expected to deliver 250 fb^{-1} of integrated luminosity to the ATLAS
 453 and CMS experiments by 2026 [29].

454 The goal of LHC physic analyses is to find and study rare events produced by interesting
 455 physics processes. The cross section σ of a given process indicates the probability of that process
 456 occurring given the beam conditions of the LHC. Multiplying the cross section by the integrated
 457 luminosity of a dataset gives the expected number of events for that process within the dataset.

$$N_{\text{events}} = \int \sigma L(t) dt = \mathcal{L} \times \sigma \quad (3.2)$$

458 The cross section for most processes of interest, especially BSM processes, is several orders of
 459 magnitude below the total cross section for the LHC. Therefore maximizing the number of events
 460 produced in collisions is crucial to increase the likelihood of producing events from processes of
 461 interest. For this reason, maximizing instantaneous luminosity is a key factor in accelerator design
 462 and operation, while mitigating the resulting pileup effects is a key component in detector design
 463 and operation.

464 **3.3 LHC Timeline**

465 The first proton-proton collisions at the LHC were achieved in 2010 with a center-of-mass
466 energy of $\sqrt{s} = 7$ TeV. Run 1 of the LHC took place between 2010 and early 2013, during which
467 time the center-of-mass collision energy increased from 7 TeV to 8 TeV. Figure 3.4 shows an
468 overview of LHC activities beginning in 2011, in the midst of Run 1. The data collected during
469 Run 1 led to the discovery of the Higgs Boston in 2012 [30].

470 Between 2013 and 2015 the LHC underwent the first Long Shutdown (LS1) during which
471 time maintenance and renovation was performed on the accelerator chain, including the repair and
472 consolidation of the high-current splices which connect the super-conducting LHC magnets. Run
473 2 of the LHC took place from 2015 to 2018 and achieved a center-of-mass energy of $\sqrt{s} = 13$ TeV.
474 Analysis of data collected in Run 2 is still on going, and is the subject of study in this thesis.

475 Between 2018 and 2022 the LHC underwent the second Long Shutdown (LS2), allowing for
476 further detector and accelerator maintenance and upgrades. Key improvements to the LHC in-
477 cluded the improvement of the insulation for over 1200 diode magnets, and the upgrade from
478 LINAC2 to LINAC4 mentioned in Section 3.1.1. Run 3 of the LHC began in 2022 and achieved a
479 center-of-mass energy of $\sqrt{s} = 13.6$ TeV.

480 Run 3 is scheduled to continue through 2026, at which point the LHC machine and detectors
481 will undergo upgrades for the *high luminosity* LHC (HL-LHC). The HL-LHC will increase the
482 instantaneous machine luminosity by a factor of 5 - 7.5 with respect to the nominal LHC design.
483 The bottom panel of Figure 3.4 shows an overview of the preparation work for the HL-LHC that
484 has been going on concurrently with Run 1, 2, and 3 of the LHC [31].



Figure 3.4: Timeline of LHC and HL-LHC activities [29]. Integrated luminosity estimates are approximate, and not reflective of the exact amount delivered to each experiment.

Chapter 4: The ATLAS Detector

487 The ATLAS detector (**A** Toroidal **L**H**C** Apparatu**S**) is one of two general purpose physics
 488 detectors designed to study the products of proton-proton collisions at the LHC. The detector is
 489 composed of a variety of specialized subsystems, designed to fully capture a wide array of physics
 490 processes. The apparatus is 25m high, 44m in length, and weighs over 7000 tons [32]. The LHC
 491 beam pipes direct proton beams to an interaction point at the center of ATLAS, and the cylindrical
 492 detector design captures a complete 360° view of the *event*, tracking all particles that result from
 493 the collision.

494 The main components of the ATLAS detector are the Inner Detector (ID) which provides high
 495 precision tracking of charged particles leaving the collision vertex, the calorimeter system which
 496 measures the energy of electromagnetic and hadronic objects, and the Muon Spectrometer (MS)
 497 which gives detailed information about muons that reach the outer radii of the detector. Two
 498 magnet systems, a 2 T solenoid magnet surrounding the ID, and a 0.5-1.0 T toroid magnet system
 499 situated throughout the MS, produce magnetic fields which bend the trajectory of charged particles
 500 traversing the detector. In addition to the main detector components, dedicated forward detectors
 501 monitor beam conditions and instantaneous luminosity, and an online trigger system reduces the
 502 data rate to a manageable level for storage. Each of these components will be discussed in further
 503 detail in this chapter.

504 4.1 Coordinate System and Geometry

505 The ATLAS detector employs a right hand cylindrical coordinate system. The z axis is aligned
 506 with the beam line, and the x-y plane sits perpendicular to the beam line. The coordinate system
 507 origin is centered on the detector, such that the origin corresponds with the interaction point of the

508 two colliding beams. The detector geometry is usually characterized by polar coordinates, where
509 the azimuthal angle ϕ spans the x-y plane. The polar angle θ represents the angle away from the
510 beam line, or z axis. $\theta = 0$ aligns with the positive z -axis, and $\phi = 0$ aligns with the positive x-axis.

511 The polar coordinate θ is generally replaced by the Lorentz invariant quantity *rapidity* or y :

$$y = \frac{1}{2} \ln\left(\frac{E + p_z}{E - p_z}\right). \quad (4.1)$$

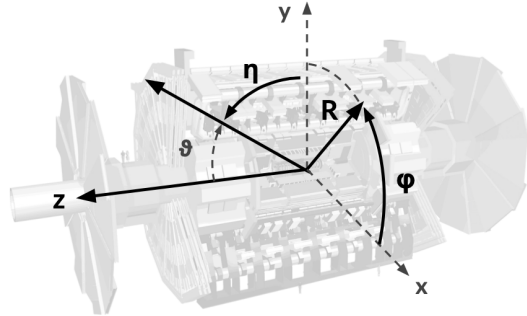
512 This substitution is advantageous because objects in the detector are traveling at highly rela-
513 tivistic speeds. The relativistic speed also means that the masses of the particles are generally small
514 compared to their total energy. In the limit of zero mass, the rapidity y reduces to the pseudorapid-
515 ity η , which can be calculated directly from the polar angle θ :

$$\eta = -\ln\left(\frac{\theta}{2}\right). \quad (4.2)$$

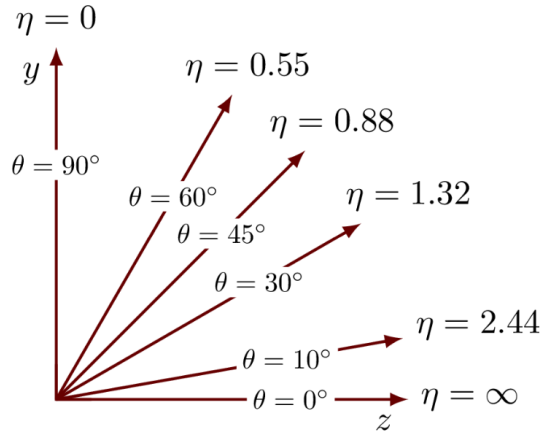
516 The distance between physics objects in the detector is generally expressed in terms of the solid
517 angle between them ΔR :

$$\Delta R = \sqrt{\Delta\phi^2 + \Delta\eta^2} \quad (4.3)$$

518 Figure 4.1a depicts the orientation of the coordinate system with respect to the ATLAS detector,
519 while Figure 4.1b illustrates the relationship between θ , η , and the beamline axis z . Direct or “head
520 on” proton-proton collisions are more likely to result in objects whose momentum is directed
521 along transverse plane (low $|\eta|$); glancing proton-proton collisions are more likely to result in
522 objects whose momentum is directed along the z -axis (high $|\eta|$). Due to the difference in the
523 nature of these collisions, as well as the cylindrical design of the ATLAS detector, the detector
524 is divided into regions of low and high η . Each subsystem has a “central” or “barrel” region
525 covering low $|\eta|$, while the “forward” or “end-cap” regions cover the area up to $|\eta| = 4.9$. Each of
526 the three main ATLAS subsystems will be discussed in the following sections.



(a) The ATLAS geometry



(b) Relationship between η and θ

Figure 4.1: ATLAS coordinate system and geometry

527 4.2 Inner Detector

528 The Inner Detector (ID) is the ATLAS subsystem closest to the interaction point. The primary
 529 purpose of the ID is to determine the charge, momentum, and trajectory of charged particles pass-
 530 ing through the detector. With this information the ID is also able to precisely determine interaction
 531 vertices.

532 The ID is composed of three sub-detectors; the Pixel Detector, the Semiconductor Tracker
 533 (SCT) and the Transition Radiation Tracker (TRT). Figure 4.2 shows the location of these three
 534 subsystems with respect to each other and the interaction point.

535 4.2.1 Pixel Detector

536 The pixel detector is the first detector encountered by particles produced in LHC collisions.
 537 The original pixel detector consists of 3 barrel layers of silicon pixels, positioned at 5 cm, 9 cm
 538 and 12 cm from the beamline. There are also 3 disks on each end-cap positioned 50 - 65 cm from
 539 the interaction point, providing full coverage for $|\eta| < 2.2$. The layers are comprised of silicon
 540 pixels each measuring $50 \times 400 \mu\text{m}^2$, with 140 million pixels in total. The pixels are organized
 541 into modules, which each contain a set of radiation hard readout electronics chips. In 2014, the
 542 Insertable B-layer (IBL) was installed, creating a new innermost layer of the pixel detector sitting

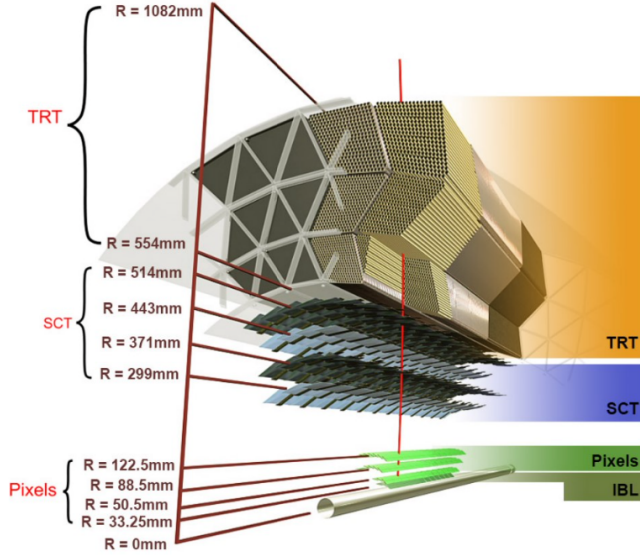


Figure 4.2: A 3D visualization of the structure of the ID in the barrel region [33]

543 just 3.3 cm from the beamline. The pixels of the IBL measure $50 \mu\text{m}$ by $250 \mu\text{m}$, and cover
 544 a pseudo-rapidity range up to $|\eta| < 3$. The IBL upgrade enhances the pixel detector's ability
 545 to reconstruct secondary vertices associated with short-lived particles such as the b-quark. The
 546 improved vertex identification also helped compensate for increasing pile-up in Run 2 [32].

547 4.2.2 Semiconductor Tracker

548 The SCT provides at least 4 additional measurements of each charged particle. It employs the
 549 same silicon technology as the Pixel Detector, but utilizes larger silicon strips which measure $80 \mu\text{m}$
 550 by 12.4 cm . The SCT is composed of 4 barrel layers, located between 30 cm and 52 cm from
 551 the beamline, and 9 end-cap layers on each side. The SCT can distinguish tracks that are separated
 552 by at least $200 \mu\text{m}$.

553 4.2.3 Transition Radiation Tracker

554 The TRT provides an additional 36 hits per particle track. The detector relies on gas filled
 555 straw tubes, a technology which is intrinsically radiation hard. The straws which are each 4 mm in
 556 diameter and up to 150 cm in length and filled with xenon gas. The detector is composed of about

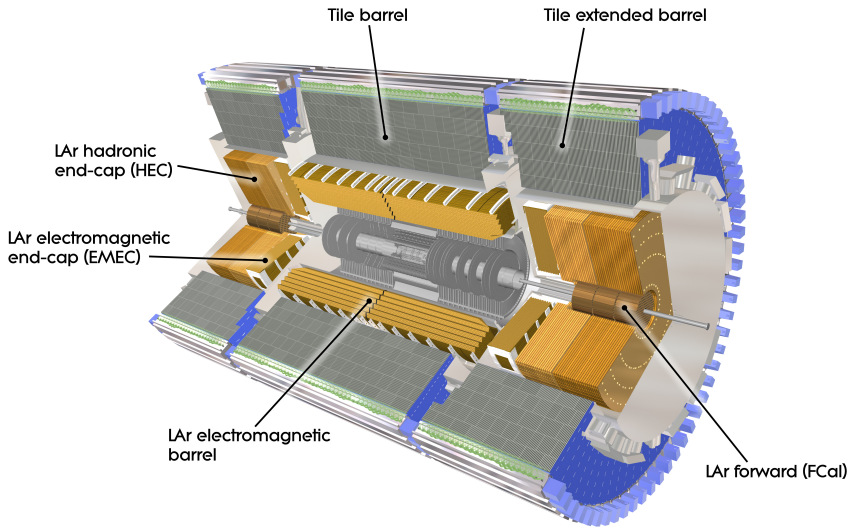


Figure 4.3: ATLAS calorimetry system [34]

557 50000 barrel region straws and 640000 end-cap straws, comprising 420000 electronic readout
 558 channels. Each channel provides a drift time measurement with a spatial resolution of $170\text{ }\mu\text{m}$ per
 559 straw. As charged particles pass through the many layers of the detector, transition radiation is
 560 emitted. The use of two different drift time thresholds allows the detector to distinguish between
 561 tracking hits and transition radiation hits.

562 4.3 Calorimeters

563 The ATLAS calorimeter system is responsible for measuring the energy of electromagnetically
 564 interacting and hadronically interacting particles passing through the detector. The calorimeters are
 565 located just outside the central solenoid magnet, which encloses the inner detectors. The calorime-
 566 ters also stop most known particles, which the exception of muons and neutrinos, preventing them
 567 from traveling to the outermost layers of the detector. The ATLAS calorimetry system is composed
 568 of two subsystems - the Liquid Argon (LAr) calorimeter for electromagnetic calorimetry and the
 569 Tile calorimeter for hadronic calorimetry. The full calorimetry system is shown in Figure 4.3.

570 4.3.1 Liquid Argon Calorimeter

571 The LAr calorimeter is a sampling calorimeter designed to trigger on and measure the ener-
572 gies of electromagnetic (EM) particles, as well as hadronic particles in the high η regions. It is
573 divided in several regions, as shown in Figure 4.3. For the region $|\eta| < 1.4$, the electromagnetic
574 barrel (EMB) is responsible for EM calorimetry, and provides high resolution energy, timing,
575 and position measurements for electrons and photons passing through the detector. The elec-
576 tromagnetic endcap (EMEC) provides additional EM calorimetry up to $|\eta| < 3.2$. In the re-
577 gion $1.4 < |\eta| < 3.2$, the hadronic endcap (HEC) provides hadronic calorimetry. For hadronic
578 calorimetry in the region $|\eta| < 1.4$, corresponding to a detector radii > 2.2 m, the less expensive
579 tile calorimeter (discussed in the next section) is used instead. A forward calorimeter (FCAL)
580 extends the hadronic calorimetry coverage up to $3.1 < |\eta| < 4.8$ [35].

581 The LAr calorimeter is composed of liquid argon sandwiched between layers of absorber mate-
582 rial and electrodes. Liquid argon is advantageous as a calorimeter active medium due to its natural
583 abundance and low cost, chemical stability, radiation tolerance, and linear response over a large
584 energy range [36]. The calorimeter is cooled to 87k by three cryostats: one barrel cryostat encom-
585 passing the EMB, and two endcap cryostats. The barrel cryostat also encloses the solenoid which
586 produces the 2T magnetic field for the inner detector. Front-end electronics are housed outside the
587 cryostats and are used to process, temporarily store, and transfer the calorimeter signals.

588 **Electromagnetic Calorimeter**

589 For the electromagnetic calorimeters, the layers of electrodes and absorber materials are ar-
590 ranged in an an accordion shape, as illustrated in Figure 4.4. The accordion shape ensures that
591 each half barrel is continuous in the azimuthal angle, which is a key feature for ensuring consistent
592 high resolution measurements. Liquid argon permeates the space between the lead absorber plates,
593 and a multilayer copper-polymide readout board runs through the center of the liquid argon filled
594 gap.

595 The detection principle for the LAr calorimeter is the current created by electrons which are

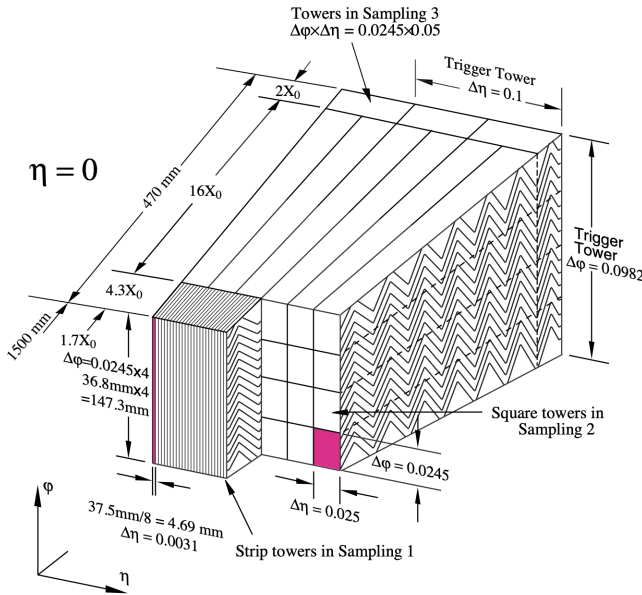


Figure 4.4: Diagram of a segment of the EMB, demonstrating the accordion plate arrangement [35]

596 released when a charged particle ionizes the liquid argon. In the barrel region, the electrons are
 597 driven towards the center electrodes by a 2000 V potential with a drift time of less than 450 ns [37].
 598 In the end-caps the voltage varies as a function of the radius in order to maintain a flat response
 599 [35]. The amount of current produced by the ionized electrons is proportional to the energy of
 600 the particle creating the signal. Figure 4.5 shows the shape of the signal produced in the LAr
 601 calorimeter, before and after it undergoes shaping during the readout process. The shaping of the
 602 pulse enforces a positive peak and a negative tail, which ensures that subsequence pulses can be
 603 separated with the precision required for the 25 ns LHC bunch spacing [35].

604 **Hadronic End-cap Calorimeter**

605 The HEC sits radially beyond the EMEC. The copper absorber plates in the HEC are oriented
 606 perpendicular to the beamline, with LAr as the active medium. Each end-cap is divided into two
 607 independent wheels; the inner wheel uses 25 mm copper plates, while the outer wheel uses 50 mm
 608 plates as a cost saving measure. In each wheel, the 8.5 mm plate gap is crossed by three parallel

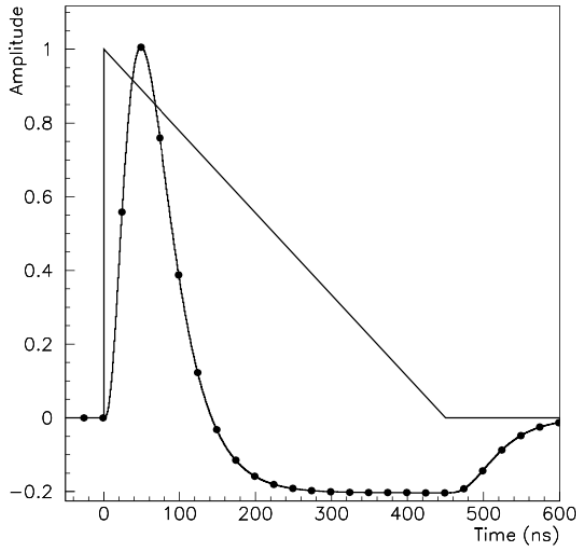


Figure 4.5: A LAr pulse as produced in the detector (triangle) and after shaping (curve) [35]

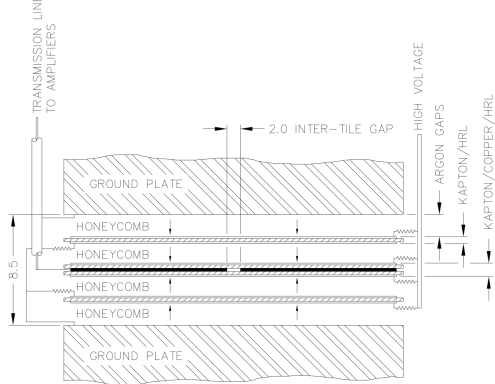


Figure 4.6: Readout gap structure in HEC [35]

609 electrodes, creating an effective drift distance of 1.8 mm. This gap is illustrated in Figure 4.6.
 610 Each wheel is divided into 32 wedge-shaped modules, each containing their own set of readout
 611 electronics.

612 **Forward Calorimeter**

613 The forward range is covered by the FCal, which provides both EM and hadronic calorimetry.
 614 It is composed of three active cylindrical modules; one EM module with copper absorber plates,
 615 and two hadronic modules with tungsten absorber plates. The plates are oriented perpendicular to

616 the beamline, and LAr is used as the active material throughout. The electrodes of the FCal consist
617 of tubes that run parallel to the beam line, arranged in a honeycomb pattern. The resulting LAr
618 gaps are as small as $250\ \mu\text{m}$, which enables the FCal to handle the large influx of particles in the
619 forward region [35].

620 4.3.2 Tile Calorimeter

621 The Tile Calorimeter (TileCal) provides hadronic calorimetry in the region $\eta < 1.7$, and sur-
622 rounds the LAr calorimeter. It is responsible for measurements of jet energy and jet substructure,
623 and also plays an important role in electron isolation and triggering (including muons) [38]. Tile-
624 Cal is composed of 3 sections, as shown in Figure 4.3; a barrel calorimeter sits directly outside the
625 LAr EMB and provides coverage up to $\eta < 1.0$. Two extended barrel sections sit outside the LAr
626 endcaps and cover the region $0.8 < \eta < 1.7$.

627 TileCal is a sampling calorimeter composed of steel and plastic scintillator plates as illustrated
628 in Figure 4.7. A total of 460,000 scintillators are read out by wavelength-shifting fibers. The
629 fibers are gathered to define cells and in turn read out by photomultiplier tubes, which amplify
630 the signal and convert it to an electrical signature. Each cell has an approximate granularity of
631 $\Delta\eta \times \Delta\phi = 0.1 \times 0.1$. Each barrel is divided azimuthally into 64 independent modules, an example
632 of which is show in Figure 4.7. The modules are each serviced by front-end electronic housed in a
633 water-cooled drawer on the exterior of the module.

634 The detection principle of the TileCal is the production of light from hadronic particles inter-
635 acting with the scintillating tiles. When a hadronic particle hits the steel plate, a shower of particles
636 are produced. The interaction of the shower with the plastic scintillator produces photons, the num-
637 ber and intensity of which are proportional to the original particle's energy.

638

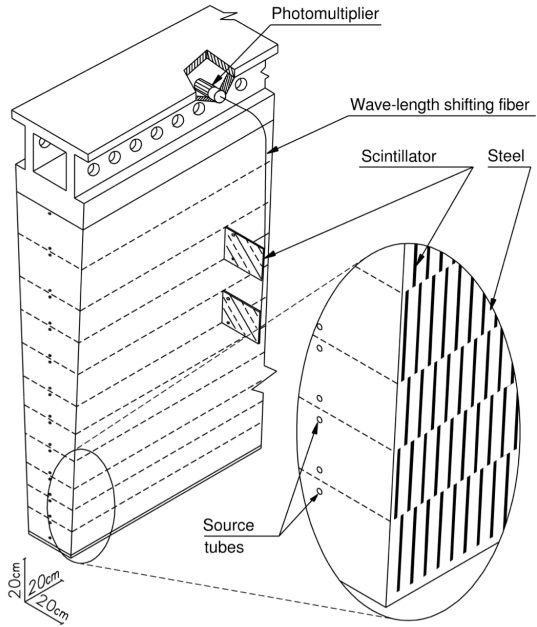


Figure 4.7: TileCal wedge module [38]

639 4.4 Muon Spectrometer

640 Unlike electrons, photons, and hadrons, muons interact minimally with the ATLAS calorimeters, and can pass through large amounts of detector material without stopping. The ATLAS Muon
 641 Spectrometer (MS) provides additional tracking information to improve the identification and measurement of muons. The MS comprises the outermost layers of the detector, and is interspersed
 642 with toroid magnets (discussed in Section 4.5), which provide a magnetic field of approximately
 643 0.5 T. The magnetic field bends the trajectory of the muons as they pass through the detector, and
 644 the degree of the bend is directly correlated with the muon momentum. The path of the muon is
 645 primarily measured by hits in three layers of Monitored Drift Tube (MDT) precision chambers,
 646 which cover the range $|\eta| < 2.7$. The barrel layout of the MS is show in Figure 4.8.

649 Muon triggering is provided by three layers of Resistive Plate Chambers (RPC) in the barrel
 650 ($|\eta| < 1.05$), and 3 - 4 layers of Thin Gap Chambers (TGC) in the end-caps ($1.05 < |\eta| < 2.4$).
 651 RPCs and TGCs also provide muon track measurements in the non-bending coordinate (ϕ). RPCs
 652 are constructed from two parallel resistive plates separated by a 2mm gap filled with a sensitive

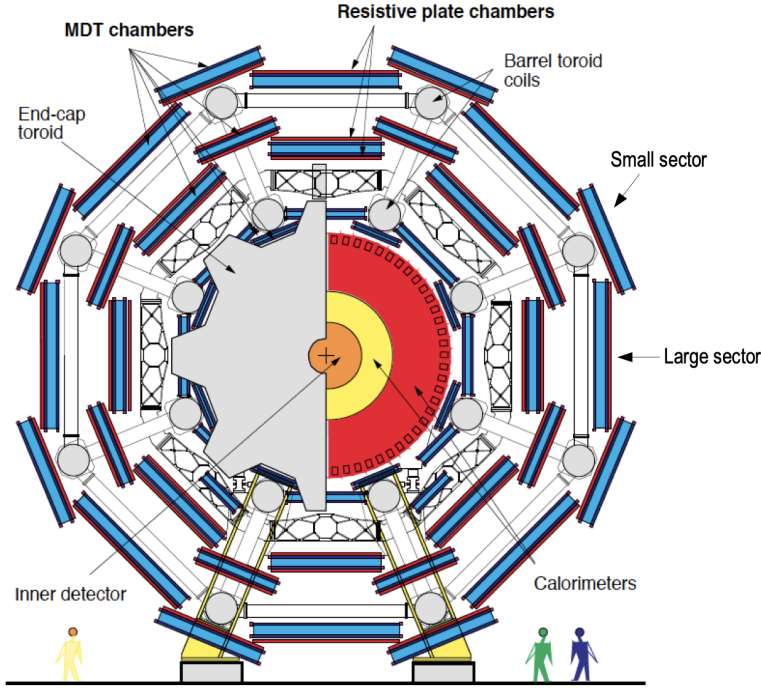


Figure 4.8: Cross section view of the muon spectrometer system [39]

653 gas mixture. This provides a total of six independent measurements for each muon track, with a
 654 spatial resolution of ~ 1 cm and a time resolution of ~ 1 ns. Time measurements from the RPCs
 655 are primarily associated to hits in the MDT precision chambers to determine the bunch crossing.
 656 The time measurement is also used to reject cosmic muons, and to search for delayed signals.
 657 TCGs provide triggering in the end-cap regions, and consist of parallel $30\ \mu\text{m}$ wires suspended
 658 in a sensitive gas mixture. TCGs provide high radiation tolerance and a fast response time, both
 659 features that are necessary for handling the high flux of muons in the forward region [39].

660 Precision measurements of muon momentum and position are primarily achieved by MDTs.
 661 The MDTs are constructed from 30 mm diameter tubes, permeated by a gas mixture of 93% Ar and
 662 7% CO₂. The average single-tube spatial resolution is $80\ \mu\text{m}$. Each chamber consists of six drift
 663 tube layers, which together provide a muon track segment resolution of $35\ \mu\text{m}$. The momentum
 664 of the muons can be calculated from the bend in the muon trajectory as they pass through the
 665 0.5T magnetic field provided by the toroids. For a $p_T = 1$ TeV track, the average p_T resolution is
 666 11%. In the inner most end-cap wheels, Cathode Strip Chambers (CSC) are used instead of MDTs,

667 covering the region $2.0 < |\eta| < 2.7$. CSCs are multi-wire proportional chambers, with a cathode
668 strip readout. The CSCs have a spatial resolution in the range of $50 \mu\text{m}$, and a maximum drift time
669 of about 30 ns, which makes them superior for handling the high flux of particles in the forward
670 region [40].

671 **4.5 Magnet System**

672 The ATLAS magnet system consists of four sets of superconducting magnets: a barrel solenoid,
673 a barrel toroid, and two end-cap toroids. The solenoid magnet produces a 2T magnetic field re-
674 sponsible for bending the trajectories of charged particles as they pass through the inner detector.
675 The three toroid magnets provide a field of 0.5 - 1 T and curve the path of muons passing through
676 the muon spectrometer.

677 The inner solenoid magnet is composed of over 9 km of niobium-titanium superconductor
678 wires, which are imbedded into strengthen pure aluminum strips. The solenoid is just 4.5 cm
679 thick, which minimizes interactions between the magnet material and particles passing through the
680 detector. It is housed in the LAr cryostat, as described in section 4.3.1, which further reduces the
681 amount of non-detector material required to support the solenoid. The return yoke of the magnet
682 is provided by the iron absorber of the TileCal [41].

683 The central ATLAS toroid magnet, providing the magnetic field for the barrel region of the MS,
684 is the largest toroidal magnet ever constructed at 25 m in length. The toroid is composed of eight
685 individual coils, each housed in their own cryostat. The toroidal magnetic field is advantageous
686 as the direction of the field is almost perpendicular to the path of the charged particles. 56 km of
687 aluminum stabilized niobium-titanium-copper superconductor wire compose the magnet. In each
688 end-cap, eight smaller superconducting coils extend the toroidal magnetic field to particles leaving
689 the detector in the forward direction [41]. Figure 4.9 shows the layout of the toroid magnets.

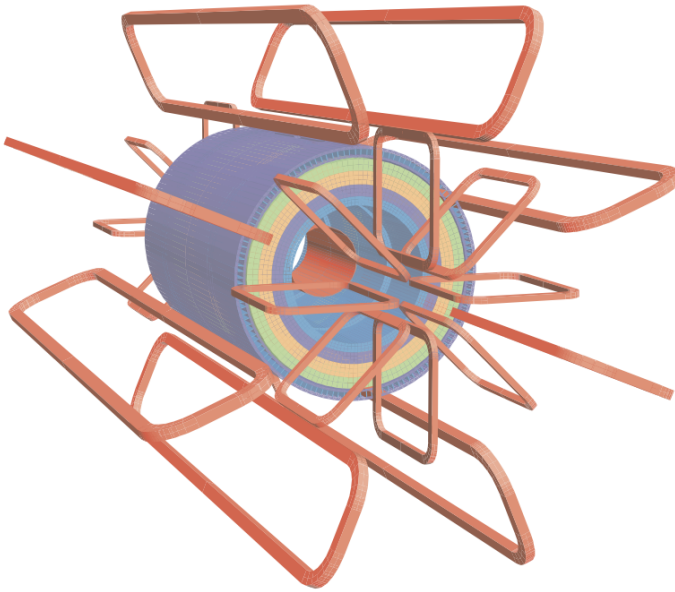


Figure 4.9: Layout of the barrel and endcap toroid magnets [32]

690 4.6 Forward Detectors

691 In addition to the inner detector, calorimeters, and muon spectrometer, three smaller detectors
692 provide coverage in the very forward region. The innermost forward detector, at 17 m from the
693 interaction point, is the **L**Uminosity measurement using **C**erenkov **I**ntegrating **D**etector (LUCID).
694 LUCID's primary purpose is to measure the relative online-luminosity for the ATLAS detector,
695 from inelastic $p - p$ scattering. The detector is composed of 20 aluminum Cerenkov tubes which
696 surround the beam pipe and face towards the interaction point.

697 The second forward detector is the Zero-Degree Calorimeter (ZDC), located 140 m from the
698 interaction point in both directions, at the point where the LHC beam-pipe divides into two separate
699 pipes. The ZDC's primary purpose is to detect forward neutrons from heavy ion collisions.

700 The third forward detector is the Absolute Luminosity For ATLAS (ALFA) system, located 240
701 m from the interaction point in both directions. ALFA determines luminosity by measuring elastic
702 scattering at small angles, from which luminosity can be calculated via the optical theorem. The
703 detector is built from scintillating fiber trackers. These are connected to the accelerator vacuum

704 via Roman pots, which allow the detector to come as close as 1mm to the beam without disrupting
705 the machine vacuum. The LUCID and ALFA detectors are crucial to determining the real-time
706 conditions of the beams and the total luminosity delivered to the ATLAS detector [32].

707 **4.7 Trigger and Data Acquisition**

708 The trigger and Data Acquisition systems (TDAQ) are responsible for selecting the most viable
709 events to save for further downstream processing. Because of the high luminosities delivered to
710 the ATLAS detector, not all events recorded can be saved; the 40 MHz bunch crossing rate must
711 be reduced by 5 orders of magnitude to an event storage rate of ~ 1 kHz. The trigger system is
712 composed of three distinct levels: Level 1 (L1), Level 2 (L2) and the event filter. Collectively the
713 L2 trigger and the event filter form the High Level Trigger (HLT).

714 The L1 trigger is implemented in the hardware of the ATLAS calorimeter and muon systems.
715 The primary modality of the L1 trigger is to identify muons, electrons, photons, jets, and τ -leptons
716 with high transverse momentum. Particles with high transverse momentum are more likely to
717 originate from direct, high energy collisions, which are most likely to produce interesting physics
718 processes. The L1 trigger also identifies events with large missing transverse energy, which could
719 be indicative of new physics. The L1 muon trigger (L1Muon) relies on RPC and TGC trigger
720 chambers in the barrel and end-cap regions of the muon spectrometer. The L1 Calorimeter Trigger
721 (L1Calo) uses reduced granularity information collected by all the calorimeter subsystems. Results
722 from the L1Muon and L1Calo triggers are combined by the Central Trigger Processor (CTP),
723 which implements a trigger ‘menu’, listing various combinations of trigger requirements. The
724 maximum L1 acceptance rate is 75 kHz, and the L1 trigger decision must reach the front-end
725 electronics within $2.5 \mu\text{s}$ of its associated bunch-crossing [32].

726 The L1 trigger defines a Region-of-Interest (RoI) for each passing event. The ROI is repre-
727 sented by the η - ϕ detector region where interesting features were identified by the L1 selection
728 process. Information about the type of feature identified and the threshold which was exceeded to
729 trigger the L1 response is also recorded. The ROI data is sent to the L2 trigger, which uses all of

730 the available information within the ROI at full granularity and precision. The L2 trigger reduces
731 the event rate from 75 kHz to 3.5 kHz, with an average processing time of 40 ms. The final stage of
732 the HLT is the event filter, which reduces the event rate to 200 Hz. The event filter uses an offline
733 analysis process to select fully rebuilt events which will be saved for further analysis.

734 All levels of the ATLAS trigger system depend on specialized electronics. Each detector front-
735 end system has a specialized Readout Driver (ROD) which collects information from several front-
736 end data streams at once. The ROD is composed of front-end analogue processing, an L1 buffer
737 which retains the information long enough for the L1 trigger decision, and dedicated links which
738 send the front-end L1 triggered data to Data Acquisition System (DAQ). Any digital signals are
739 formatted as raw data before being transferred to the DAQ. The first stage of the DAQ temporarily
740 stores the L1 data in local buffers. The ROI data is then requested by the L2 trigger, after which
741 selected events are transferred to an event building system, before events passing the event filter
742 are sent to the CERN computer center for permanent storage. The DAQ system not only allows
743 for the readout of detector data, but is also responsible for the monitoring and configuration of
744 the hardware and software components which make up the data readout system via the Detector
745 Control System (DCS).

746 The DCS allows centralized control of all detector subsystems simultaneously. It continually
747 monitors operational conditions, reports any abnormal behavior to the operator, and can perform
748 both automatic and manual interventions. The DCS reports on real time detector conditions such
749 as high or low voltage detector electronics, gas and cooling systems, magnetic field conditions,
750 humidity and temperature. This information is continually monitored by experts in the ATLAS
751 control room, so that action can be taken immediately to correct any issues that arise. The DCS also
752 handles communication between detector systems, and other systems such as the LHC accelerator,
753 the ATLAS magnets, and CERN technical services [32].

Chapter 5: Particle Reconstruction and Identification

756 With a design luminosity of $1.0 \times 10^{34} \text{ cm}^{-2}\text{s}^{-1}$, and a peak Run-2 instantaneous luminosity of
 757 $2.0 \times 10^{34} \text{ cm}^{-2}\text{s}^{-1}$, reconstructing and identifying the products of LHC pp collisions is one of the
 758 most complex tasks for each LHC experiment. The accurate reconstruction and identification of
 759 physics objects lays the ground work for all subsequent physics analyses, so it is also one of the
 760 most fundamentally important tasks performed by an experiment.

761 Reconstruction is the process of combining raw and uncalibrated hits across various subsys-
 762 tems into specific unique objects. Two particular subsystems, the Inner Detector (ID) tracker and
 763 the calorimeter play particularly important roles and will be discussed in detail. Analysis of the
 764 properties of the reconstructed objects identifies them as photon, electrons, muons, or jets. While
 765 photons, electrons, and muons are fundamental particles, jets represent a collimated shower of
 766 many hadronic particles, whose definition is more flexible. Jet reconstruction, clustering and sub-
 767 structure are all of particular important to jet identification, and to the later content of this thesis.
 768 Finally, reconstruction also identifies missing transverse energy E_T^{miss} in events, which is a crucial
 769 variable for BSM physics searches. Figure 5.1 shows how the various physics objects listed here
 770 interact with various systems in the ATLAS detector.

771 5.1 Inner Detector Tracks

772 As the inner most layer of the detector, the ID measures charged particles close to the interac-
 773 tion point. The various hits of these charged particles throughout the ID are used to reconstruct
 774 *tracks* which give the trajectories of charged particles. Track reconstruction begins by clustering
 775 hits in the Pixel and SCT detectors, and combining clusters from different radial layers of these de-
 776 tector. The multi-layer clusters form track *seeds*, which provide initial estimates of measurements

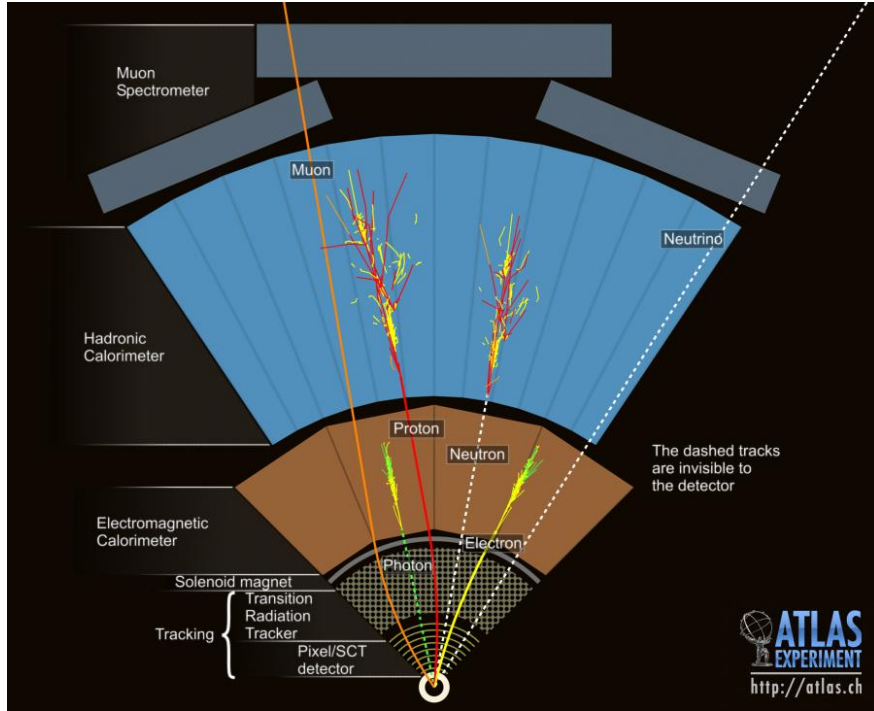


Figure 5.1: Graphic illustrating the various objects and high level features identified by ATLAS object reconstruction, and their interaction with different systems of the ATLAS detector [42]

777 belonging to an individual track. The requirement of three points allows for a rough estimate of
 778 the track p_T to be made by calculating the curvature of the track and accounting of the magnetic
 779 field in the ID.

780 Tracks seeds are subject to a variety of quality requirements, such as having a minimum esti-
 781 mated p_T and passing interaction region compatibility criterion. If these requirements are satisfied,
 782 the track seeds are passed to the track finding and fitting algorithms. The interplay of these three
 783 track reconstruction steps is illustrated in Figure 5.2.

784 5.2 Photons and Electrons

785 Photons and electrons shower in the LAr calorimeter, and are identified by the energy deposits
 786 they leave there. Energy deposits in a collection of nearby cells are termed *clusters*, which become
 787 the starting point for electron and photon reconstruction [44]. The clustering algorithm begins
 788 when the energy deposit in a certain cell exceeds the noise threshold with a significance of 4σ .

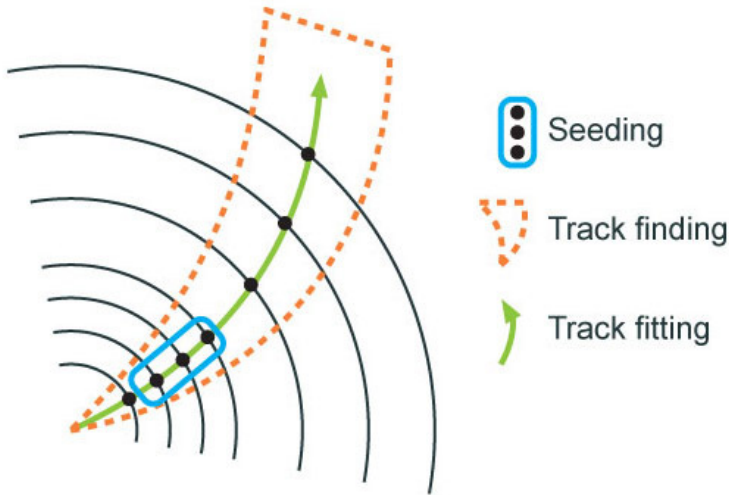


Figure 5.2: Track reconstruction seeding, finding and fitting illustration [43]

789 The algorithm then collects neighboring cells which have an energy deposit exceeding the noise
 790 threshold with a significance of 2σ , creating a topo-cluster. Next, these topo-clusters are matched
 791 to ID tracks, created as described in Section 5.1. The location of the topo-cluster defines a region
 792 of interest (ROI) in the ID, where additional modified track reconstruction algorithms are run in the
 793 case that no associated tracks are found. Any ID tracks associated to the topo-cluster are retrofitted to
 794 allow for additional energy loss due to bremsstrahlung. A converted photon track reconstruction
 795 algorithm is run to check for tracks coming from secondary vertices consistent with converted
 796 photons. The secondary vertices are constructed from two opposite charged tracks consistent with
 797 a massless particle, or from one track without any hits in the innermost layer of the ID.

798 For electron identification, the EM cluster is required to match ID tracks that originate from
 799 the primary vertex at the interaction point. For photon identification, the EM cluster can either be
 800 matched to tracks coming from a secondary vertex (converted photon), or matched to no tracks
 801 (unconverted photon). Figure 5.3 illustrates these three cases for EM object identification.

802 *Superclusters* are built separately for photons and electrons, based on the combined topo-cluster
 803 and ID track information. First, the EM topo-clusters are tested to see if they meet the minimum
 804 requirements to become electron or photon seed clusters. For electrons, the cluster must have a
 805 minimum E_T of 1 GeV, and must be matched to a track with at least 4 hits in the silicon tracking

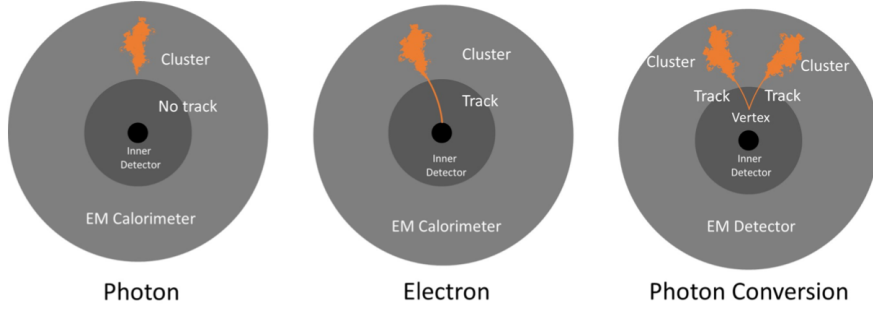


Figure 5.3: Four types of muon track candidates [45].

detectors. For photons, the cluster must have an E_T greater than 1.5 GeV. If the seed cluster requirements are met, the algorithm searches for satellite clusters, which can arise from bremsstrahlung radiation. If the satellite clusters pass the positional, energy and tracking requirements to be associated with the proto-cluster, they are combined into a supercluster.

Electron and photon objects are identified from the superclusters after energy calibration and position corrections are applied. Because photon and electron superclusters are built independently, some clusters can produce both a photon and an electron. In this case an ambiguity resolution procedure is applied to determine if the supercluster can be easily identified as only a photon (no tracks present) or only an electron (good tracks pointing to the primary vertex). In some cases, the identity of the cluster is still ambiguous, in which case both a photon and electron object are created for analysis and flagged as ambiguous. Energy, shower shape, and other analysis variables are calculated from the supercluster and saved with the electron or photon object.

5.3 Muons

Muons are identified through the tracks and energy deposits they leave in the ID, calorimeters, and Muon Spectrometer (MS). Muon identification begins in the Muon Drift Tube chambers by performing a straight line fit between the hits found in each layer, creating *segments*. Segments in the middle layers are then used as seeds for the track building algorithm, which searches for compatible combinations of segments based on their relative positions and angles. A χ^2 fit is

824 performed on each track candidate [46]. Based on the χ^2 criteria, hits are removed or added such
825 that the track contains as many hits as possible while satisfying the fit criteria.

826 The MS track candidates are combined with track information from the ID and calorimeters
827 according to various algorithms based on the information available from each subdetector. Four
828 different types of muons arise from the various reconstruction algorithms:

- 829 • Combined muon: a muon track identified through independent track reconstruction in the
830 ID and MS, where the combined track is formed using a global refit that uses hit information
831 from both detectors. Most muons are constructed through an outside-in procedure, in which
832 a muon track candidate is identified in the MS and then an associated track is found in the ID.
833 A complementary inside-out procedure is also implemented and identifies additional muons.
- 834 • Segment-tagged muon: an ID track is identified as a muon if when extrapolated out to the
835 MS (following the inside-out global fit procedure) it is matched to at least one local MS
836 segment.
- 837 • Calorimeter-tagged muon: an ID track is identified as a muon if it is matched to a calorimeter
838 energy deposit that is compatible with a minimum-ionizing particle. This muon identifica-
839 tion has the lowest purity, but it used in regions where the MS has only partial coverage due
840 to cabling and service access routes.
- 841 • Extrapolated muons: the muon is reconstruction only from the MS track and a requirement
842 on compatibility with the primary interaction point. The muon track is required to cross at
843 least two layers of the MS, and three layers in the forward region. These muons are mainly
844 used to extend muon acceptance into the region $2.5 < |\eta| < 2.7$ where ID track information
845 is not available.

846 Figure 5.4 illustrates the four types of muon reconstruction. Overlap between reconstructed
847 muons using ID tracks is resolved by giving preference to combined muons, then segment tagged
848 muons, and finally calorimeter tagged muons. Overlap with extrapolated muons is resolved by
849 giving preference to the muon with a better fit quality and higher number of tracks.

850 All muon track candidates are required to pass a series of quality selections to be identified in
 851 the final muon collection. The primary qualities considered are the χ^2 goodness of fit for the global
 852 track, the difference in p_T measurement between the ID and MS tracks, and the ratio between the
 853 charge and momentum of the tracks. The quality requirements help reject hadrons, primarily from
 854 kaon and pion decays. Muons candidates consistent with cosmic rays are also rejected.

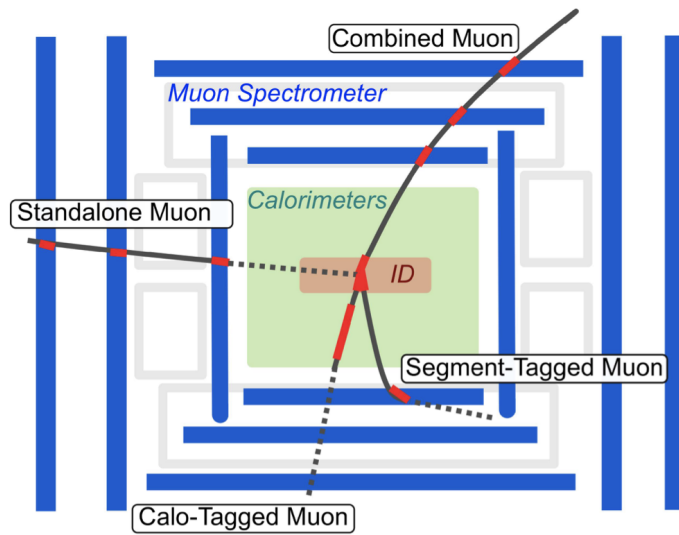


Figure 5.4: Four types of muon track candidates [47].

855 5.4 Jets

856 The protons accelerated in the LHC are composed of quarks and gluons, and thus their colli-
 857 sions often result in the release of energetic quarks and gluons, collectively termed *partons*. The
 858 energetic partons can radiate additional gluons, and these gluons can pair produce quarks in a pro-
 859 cess called *fragmentation*. Fragmentation continues until the energy drops sufficiently that color
 860 conservation plays a dominant role. At that point, additional quarks and gluons are produced from
 861 vacuum to create neutral color states for the fragmented collection of partons. This process is
 862 known as *hadronization* [48]. The hadronized partons compose a collimated stream of particles,
 863 known as a *jet*, which is then observed in the detector. The full process that produces jets is known
 864 as a *parton shower*, and is illustrated in Figure 5.5.

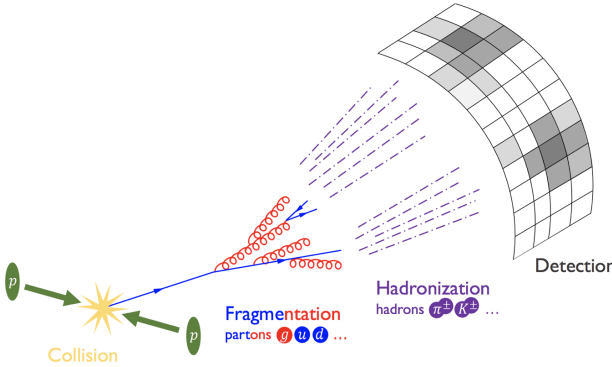


Figure 5.5: The fragmentation and hadronization processes undergone by a quark produced in a proton-proton collision [49].

865 Jets are identified by the energy deposits they leave in the calorimeter, which are then matched
 866 to the tracks they leave in the ID. Jet reconstruction generally begins in the calorimeters, with the
 867 identification of *topo-clusters*. Then jet reconstruction algorithms combine calorimeter informa-
 868 tion with tracking information. The anti- k_t algorithm [50] as provided by the FastJet library [51] is
 869 generally used by the ATLAS experiment, with varying reconstruction radius settings. There are a
 870 variety of jet collections depending on the exact usage of calorimeter and tracking information in
 871 the reconstruction. Some common collections include particle flow jets(PFlow), track calo-cluster
 872 jets (TCC), EM topo-cluster jets (EMTopo), and unified flow object jets (UFO). Only particle flow
 873 jets will be discussed in greater detail due to their importance in this analysis. The following sec-
 874 tions discuss jet identification in the calorimeters, particle flow jet construction using the anti- k_t
 875 algorithm, jet clustering and jet substructure characteristics.

876 5.4.1 Calorimeter Clusters

877 5.4.2 Particle Flow Reconstruction

878 5.4.3 Jet Clustering

879 5.4.4 Jet Substructure

880 **5.5 Missing Transverse Energy**

Conclusion or Epilogue

882 Use this page for your epilogue or conclusion if applicable; please use only one of the titles
883 for this page. Otherwise, you may delete it. Use this page for your epilogue or conclusion if
884 applicable; please use only one of the titles for this page. Otherwise, you may delete it. Use this
885 page for your epilogue or conclusion if applicable; please use only one of the titles for this page.
886 Otherwise, you may delete it. Use this page for your epilogue or conclusion if applicable; please
887 use only one of the titles for this page. Otherwise, you may delete it. Use this page for your
888 epilogue or conclusion if applicable; please use only one of the titles for this page. Otherwise,
889 you may delete it. Use this page for your epilogue or conclusion if applicable; please use only one
890 of the titles for this page. Otherwise, you may delete it. Use this page for your epilogue or
891 conclusion if applicable; please use only one of the titles for this page. Otherwise, you may delete
892 it. Use this page for your epilogue or conclusion if applicable; please use only one of the titles for
893 this page. Otherwise, you may delete it. Use this page for your epilogue or conclusion if
894 applicable; please use only one of the titles for this page. Otherwise, you may delete it. Use this
895 page for your epilogue or conclusion if applicable; please use only one of the titles for this page.
896 Otherwise, you may delete it. Use this page for your epilogue or conclusion if applicable; please
897 use only one of the titles for this page. Otherwise, you may delete it. Use this page for your
898 epilogue or conclusion if applicable; please use only one of the titles for this page. Otherwise,
899 you may delete it. Use this page for your epilogue or conclusion if applicable; please use only one
900 of the titles for this page. Otherwise, you may delete it. Use this page for your epilogue or
901 conclusion if applicable; please use only one of the titles for this page. Otherwise, you may delete

902 it. Use this page for your epilogue or conclusion if applicable; please use only one of the titles for
903 this page. Otherwise, you may delete it. Use this page for your epilogue or conclusion if
904 applicable; please use only one of the titles for this page. Otherwise, you may delete it. Use this
905 page for your epilogue or conclusion if applicable; please use only one of the titles for this page.
906 Otherwise, you may delete it. Use this page for your epilogue or conclusion if applicable; please
907 use only one of the titles for this page. Otherwise, you may delete it. Use this page for your
908 epilogue or conclusion if applicable; please use only one of the titles for this page. Otherwise,
909 you may delete it. Use this page for your epilogue or conclusion if applicable; please use only one
910 of the titles for this page. Otherwise, you may delete it. Use this page for your epilogue or
911 conclusion if applicable; please use only one of the titles for this page. Otherwise, you may delete
912 it. Use this page for your epilogue or conclusion if applicable; please use only one of the titles for
913 this page. Otherwise, you may delete it. Use this page for your epilogue or conclusion if
914 applicable; please use only one of the titles for this page. Otherwise, you may delete it. Use this
915 page for your epilogue or conclusion if applicable; please use only one of the titles for this page.
916 Otherwise, you may delete it. Use this page for your epilogue or conclusion if applicable; please
917 use only one of the titles for this page. Otherwise, you may delete it. Use this page for your
918 epilogue or conclusion if applicable; please use only one of the titles for this page. Otherwise,
919 you may delete it. Use this page for your epilogue or conclusion if applicable; please use only one
920 of the titles for this page. Otherwise, you may delete it. Use this page for your epilogue or
921 conclusion if applicable; please use only one of the titles for this page. Otherwise, you may delete
922 it. Use this page for your epilogue or conclusion if applicable; please use only one of the titles for
923 this page. Otherwise, you may delete it. Use this page for your epilogue or conclusion if
924 applicable; please use only one of the titles for this page. Otherwise, you may delete it. Use this
925 page for your epilogue or conclusion if applicable; please use only one of the titles for this page.
926 Otherwise, you may delete it. Use this page for your epilogue or conclusion if applicable; please
927 use only one of the titles for this page. Otherwise, you may delete it. Use this page for your
928 epilogue or conclusion if applicable; please use only one of the titles for this page. Otherwise,

929 you may delete it. Use this page for your epilogue or conclusion if applicable; please use only one
930 of the titles for this page. Otherwise, you may delete it. Use this page for your epilogue or
931 conclusion if applicable; please use only one of the titles for this page. Otherwise, you may delete
932 it. Use this page for your epilogue or conclusion if applicable; please use only one of the titles for
933 this page. Otherwise, you may delete it. Use this page for your epilogue or conclusion if
934 applicable; please use only one of the titles for this page. Otherwise, you may delete it. Use this
935 page for your epilogue or conclusion if applicable; please use only one of the titles for this page.
936 Otherwise, you may delete it. Use this page for your epilogue or conclusion if applicable; please
937 use only one of the titles for this page. Otherwise, you may delete it. Use this page for your
938 epilogue or conclusion if applicable; please use only one of the titles for this page. Otherwise,
939 you may delete it. Use this page for your epilogue or conclusion if applicable; please use only one
940 of the titles for this page. Otherwise, you may delete it. Use this page for your epilogue or
941 conclusion if applicable; please use only one of the titles for this page. Otherwise, you may delete
942 it. Use this page for your epilogue or conclusion if applicable; please use only one of the titles for
943 this page. Otherwise, you may delete it. Use this page for your epilogue or conclusion if
944 applicable; please use only one of the titles for this page. Otherwise, you may delete it. Use this
945 page for your epilogue or conclusion if applicable; please use only one of the titles for this page.
946 Otherwise, you may delete it. Use this page for your epilogue or conclusion if applicable; please
947 use only one of the titles for this page. Otherwise, you may delete it. Use this page for your
948 epilogue or conclusion if applicable; please use only one of the titles for this page. Otherwise,
949 you may delete it. Use this page for your epilogue or conclusion if applicable; please use only one
950 of the titles for this page. Otherwise, you may delete it. Use this page for your epilogue or
951 conclusion if applicable; please use only one of the titles for this page. Otherwise, you may delete
952 it. Use this page for your epilogue or conclusion if applicable; please use only one of the titles for
953 this page. Otherwise, you may delete it. Use this page for your epilogue or conclusion if
954 applicable; please use only one of the titles for this page. Otherwise, you may delete it. Use this
955 page for your epilogue or conclusion if applicable; please use only one of the titles for this page.

956 Otherwise, you may delete it. Use this page for your epilogue or conclusion if applicable; please
957 use only one of the titles for this page. Otherwise, you may delete it. Use this page for your
958 epilogue or conclusion if applicable; please use only one of the titles for this page. Otherwise,
959 you may delete it. Use this page for your epilogue or conclusion if applicable; please use only one
960 of the titles for this page. Otherwise, you may delete it. Use this page for your epilogue or
961 conclusion if applicable; please use only one of the titles for this page. Otherwise, you may delete
962 it. Use this page for your epilogue or conclusion if applicable; please use only one of the titles for
963 this page. Otherwise, you may delete it. Use this page for your epilogue or conclusion if
964 applicable; please use only one of the titles for this page. Otherwise, you may delete it. Use this
965 page for your epilogue or conclusion if applicable; please use only one of the titles for this page.
966 Otherwise, you may delete it. Use this page for your epilogue or conclusion if applicable; please
967 use only one of the titles for this page. Otherwise, you may delete it. Use this page for your
968 epilogue or conclusion if applicable; please use only one of the titles for this page. Otherwise,
969 you may delete it. Use this page for your epilogue or conclusion if applicable; please use only one
970 of the titles for this page. Otherwise, you may delete it. Use this page for your epilogue or
971 conclusion if applicable; please use only one of the titles for this page. Otherwise, you may delete
972 it. Use this page for your epilogue or conclusion if applicable; please use only one of the titles for
973 this page. Otherwise, you may delete it. Use this page for your epilogue or conclusion if
974 applicable; please use only one of the titles for this page. Otherwise, you may delete it. Use this
975 page for your epilogue or conclusion if applicable; please use only one of the titles for this page.
976 Otherwise, you may delete it. Use this page for your epilogue or conclusion if applicable; please
977 use only one of the titles for this page. Otherwise, you may delete it. Use this page for your
978 epilogue or conclusion if applicable; please use only one of the titles for this page. Otherwise,
979 you may delete it. Use this page for your epilogue or conclusion if applicable; please use only one
980 of the titles for this page. Otherwise, you may delete it. Use this page for your epilogue or
981 conclusion if applicable; please use only one of the titles for this page. Otherwise, you may delete
982 it.

References

- [1] Jens Erler and Paul Langacker. “Electroweak model and constraints on new physics”. In: (July 2004). arXiv: hep-ph/0407097.
- [2] David J Griffiths. *Introduction to elementary particles; 2nd rev. version*. Physics textbook. New York, NY: Wiley, 2008.
- [3] M. Tanabashi et al. “Review of Particle Physics”. In: *Phys. Rev. D* 98 (3 2018), pp. 847–851.
- [4] E. Noether. “Invariante Variationsprobleme”. In: *Nachr. d. König. Gesellsch. d. Wiss. zu Göttingen, Math-phys. Klasse*, Seite 235-157 (1918). eprint: www.physics.ucla.edu/\~\cwp/articles/noether.trans/german/emmy235.html.
- [5] J. H. Christenson et al. “Evidence for the 2π Decay of the K_2^0 Meson”. In: *Phys. Rev. Lett.* 13 (1964), pp. 138–140.
- [6] J. E. Augustin et al. “Discovery of a Narrow Resonance in e^+e^- Annihilation”. In: *Phys. Rev. Lett.* 33 (1974), pp. 1406–1408.
- [7] J. J. Aubert et al. “Experimental Observation of a Heavy Particle J ”. In: *Phys. Rev. Lett.* 33 (1974), pp. 1404–1406.
- [8] Martin L. Perl et al. “Evidence for Anomalous Lepton Production in e+ - e- Annihilation”. In: *Phys. Rev. Lett.* 35 (1975), pp. 1489–1492.
- [9] S. W. Herb et al. “Observation of a Dimuon Resonance at 9.5-GeV in 400-GeV Proton-Nucleus Collisions”. In: *Phys. Rev. Lett.* 39 (1977), pp. 252–255.
- [10] F. Abe et al. “Observation of top quark production in $\bar{p}p$ collisions”. In: *Phys. Rev. Lett.* 74 (1995), pp. 2626–2631. arXiv: hep-ex/9503002.
- [11] S. Abachi et al. “Observation of the top quark”. In: *Phys. Rev. Lett.* 74 (1995), pp. 2632–2637. arXiv: hep-ex/9503003.
- [12] K. Kodama et al. “Observation of tau neutrino interactions”. In: *Phys. Lett. B* 504 (2001), pp. 218–224. arXiv: hep-ex/0012035.
- [13] G. Arnison et al. “Experimental Observation of Lepton Pairs of Invariant Mass Around 95-GeV/c**2 at the CERN SPS Collider”. In: *Phys. Lett. B* 126 (1983), pp. 398–410.

- 1010 [14] P. Bagnaia et al. “Evidence for $Z^0 \rightarrow e^+e^-$ at the CERN $\bar{p}p$ Collider”. In: *Phys. Lett. B* 129
1011 (1983), pp. 130–140.
- 1012 [15] Serguei Chatrchyan et al. “Observation of a New Boson at a Mass of 125 GeV with the
1013 CMS Experiment at the LHC”. In: *Phys. Lett. B* 716 (2012), pp. 30–61. arXiv: 1207.7235
1014 [hep-ex].
- 1015 [16] Georges Aad et al. “Observation of a new particle in the search for the Standard Model
1016 Higgs boson with the ATLAS detector at the LHC”. In: *Phys. Lett. B* 716 (2012), pp. 1–29.
1017 arXiv: 1207.7214 [hep-ex].
- 1018 [17] K. G. Begeman, A. H. Broeils, and R. H. Sanders. “Extended rotation curves of spiral galax-
1019 ies: Dark haloes and modified dynamics”. In: *Mon. Not. Roy. Astron. Soc.* 249 (1991), p. 523.
- 1020 [18] Y. Ashie et al. “Evidence for an oscillatory signature in atmospheric neutrino oscillation”.
1021 In: *Phys. Rev. Lett.* 93 (2004), p. 101801. arXiv: hep-ex/0404034.
- 1022 [19] C. Abel et al. “Measurement of the Permanent Electric Dipole Moment of the Neutron”. In:
1023 *Phys. Rev. Lett.* 124.8 (2020), p. 081803. arXiv: 2001.11966 [hep-ex].
- 1024 [20] Guillaume Albouy et al. “Theory, phenomenology, and experimental avenues for dark show-
1025 ers: a Snowmass 2021 report”. In: *The European Physical Journal C* 82.12 (Dec. 2022).
- 1026 [21] Lyndon Evans and Philip Bryant. “LHC Machine”. In: *Journal of Instrumentation* 3.08
1027 (2008), S08001.
- 1028 [22] “The ATLAS Experiment at the CERN Large Hadron Collider”. In: *JINST* 3 (2008). Also
1029 published by CERN Geneva in 2010, S08003.
- 1030 [23] “The CMS experiment at the CERN LHC”. In: *Journal of Instrumentation* 3.08 (2008),
1031 S08004.
- 1032 [24] “The ALICE experiment at the CERN LHC”. In: *Journal of Instrumentation* 3.08 (2008),
1033 S08002.
- 1034 [25] “The LHCb Detector at the LHC”. In: *Journal of Instrumentation* 3.08 (2008), S08005.
- 1035 [26] Ana Lopes and Melissa Loyse Perrey. *FAQ-LHC The guide*. 2022.
- 1036 [27] Esma Mobs. “The CERN accelerator complex in 2019. Complexe des accélérateurs du
1037 CERN en 2019”. In: (2019). General Photo.
- 1038 [28] *Pulling together: Super Conducting electromagnets*. <https://home.cern/science/engineering/pulling-together-superconducting-electromagnets>.
1039 Accessed: 2024-01-05.

- 1041 [29] *The High-Luminosity LHC*. <https://voisins.web.cern.ch/en/high-luminosity-lhc-hl-lhc>. Accessed: 2024-01-05.
- 1042
- 1043 [30] Aad G., et al. (ATLAS Collaboration and CMS Collaboration). “Combined Measurement of
1044 the Higgs Boson Mass in pp Collisions at $\sqrt{s} = 7$ and 8 TeV with the ATLAS and CMS
1045 Experiments”. In: *Phys. Rev. Lett.* 114 (19 2015), p. 191803.
- 1046 [31] O. Aberle et al. *High-Luminosity Large Hadron Collider (HL-LHC): Technical design re-*
1047 *port*. CERN Yellow Reports: Monographs. Geneva: CERN, 2020.
- 1048 [32] The ATLAS Collaboration. “The ATLAS Experiment at the CERN Large Hadron Collider”.
1049 In: *Journal of Instrumentation* 3.08 (2008), S08003.
- 1050 [33] G Aad, B Abbott, and ATLAS Collaboration. “Performance of the reconstruction of large
1051 impact parameter tracks in the inner detector of ATLAS”. In: *Eur. Phys. J. C Part. Fields*
1052 83.11 (Nov. 2023).
- 1053 [34] Joao Pequenao. *Computer Generated image of the ATLAS calorimeter*. 2008.
- 1054 [35] *ATLAS liquid-argon calorimeter: Technical Design Report*. Technical design report. AT-
1055 LAS. Geneva: CERN, 1996.
- 1056 [36] H A Gordon. “Liquid argon calorimetry for the SSC”. In: () .
- 1057 [37] Henric Wilkens and (on behalf of the ATLAS LArg Collaboration). “The ATLAS Liquid
1058 Argon calorimeter: An overview”. In: *Journal of Physics: Conference Series* 160.1 (2009),
1059 p. 012043.
- 1060 [38] *Technical Design Report for the Phase-II Upgrade of the ATLAS Tile Calorimeter*. Tech.
1061 rep. Geneva: CERN, 2017.
- 1062 [39] “Technical Design Report for the Phase-II Upgrade of the ATLAS Muon Spectrometer”. In:
1063 () .
- 1064 [40] L Pontecorvo. “The ATLAS Muon Spectrometer”. In: (2004). revised version number 1
1065 submitted on 2003-07-27 16:31:16.
- 1066 [41] *ATLAS magnet system: Technical Design Report, 1*. Technical design report. ATLAS. Geneva:
1067 CERN, 1997.
- 1068 [42] Joao Pequenao. “Event Cross Section in a computer generated image of the ATLAS detec-
1069 tor.” 2008.
- 1070 [43] ATLAS Collaboration. “ATLAS Experiment Implements Heterogeneous Particle Recon-
1071 struction with Intel oneAPI Tools”. General Photo. 2023.

- 1072 [44] ATLAS Collaboration. “Electron and photon performance measurements with the ATLAS
1073 detector using the 2015–2017 LHC proton-proton collision data”. In: *Journal of Instrumentation*
1074 14.12 (2019), P12006.
- 1075 [45] Chiara Deponte. “Studies on the properties of non-prompt photons at the ATLAS experi-
1076 ment”. Presented 16 Aug 2022. Technische Universitaet Dortmund (DE), 2022.
- [46] ATLAS Collaboration. “Muon reconstruction performance of the ATLAS detector in pro-
ton–proton collision data at
 \sqrt{s}
1077 $s = 13 \text{ TeV}$ ”. In: *The European Physical Journal C* 76.5 (2016).
- 1078 [47] Sebastien Rettie. *Muon identification and performance in the ATLAS experiment*. Tech. rep.
1079 Geneva: CERN, 2018.
- 1080 [48] B. R. Webber. *Fragmentation and Hadronization*. 1999. arXiv: hep-ph/9912292 [hep-ph].
- 1081 [49] Eric M. Metodiev. *The Fractal Lives of Jets* | Eric M. Metodiev — ericmetodiev.com. <https://www.ericmetodiev.com/post/jetformation/>. 2019, note = [Accessed 18-
1082 05-2024],
- 1083
- 1084 [50] Matteo Cacciari, Gavin P Salam, and Gregory Soyez. “The anti-k_Tjet clustering algorithm”.
1085 In: *Journal of High Energy Physics* 2008.04 (Apr. 2008), 063–063.
- 1086 [51] Matteo Cacciari, Gavin P. Salam, and Gregory Soyez. “FastJet user manual: (for version
1087 3.0.2)”. In: *The European Physical Journal C* 72.3 (Mar. 2012).

1088

1089

Appendix A: Experimental Equipment

1090 Lorem ipsum dolor sit amet, consectetur adipiscing elit, sed do eiusmod tempor incididunt ut
1091 labore et dolore magna aliqua. Ut enim ad minim veniam, quis nostrud exercitation ullamco laboris
1092 nisi ut aliquip ex ea commodo consequat. Duis aute irure dolor in reprehenderit in voluptate velit
1093 esse cillum dolore eu fugiat nulla pariatur. Excepteur sint occaecat cupidatat non proident, sunt in
1094 culpa qui officia deserunt mollit anim id est laborum.

1095

1096

Appendix B: Data Processing

1097 Lorem ipsum dolor sit amet, consectetur adipiscing elit, sed do eiusmod tempor incididunt ut
1098 labore et dolore magna aliqua. Ut enim ad minim veniam, quis nostrud exercitation ullamco laboris
1099 nisi ut aliquip ex ea commodo consequat. Duis aute irure dolor in reprehenderit in voluptate velit
1100 esse cillum dolore eu fugiat nulla pariatur. Excepteur sint occaecat cupidatat non proident, sunt in
1101 culpa qui officia deserunt mollit anim id est laborum.